Muscle Torque Generator Model For A Two Degree-of-Freedom Shoulder Joint

by

Sydney Bell

A thesis
presented to the University of Waterloo
in fulfillment of the
thesis requirement for the degree of
Master of Applied Science
in
Systems Design Engineering

Waterloo, Ontario, Canada, 2023

Author's Declaration

I hereby declare that I am the sole author of this thesis. This is a true copy of the thesis, including any required final revisions, as accepted by my examiners.

I understand that my thesis may be made electronically available to the public.

Abstract

Muscle Torque Generators (MTGs) have been developed as an alternative to muscle-force models, reducing the complexity of muscle-force models to a single torque at the joint. Previous studies have been conducted to determine functions to scale joint torque based on position and velocity-dependent properties. However, current MTGs can only be applied to single Degree of Freedom (DOF) joints, leading to complications in modeling joints such as the shoulder, which has 3 DOF. Therefore, this project aimed to develop, for the first time, an MTG model that accounts for the coupling between 2 DOF at the shoulder joint, with shoulder plane of elevation and shoulder elevation being the DOF of interest.

The 2 DOF MTG form was based on previous research for a single DOF MTG. Three different 2 DOF MTG equations were developed to evaluate the effect of the degree of coupling between DOF. Polynomial torque-angle scaling, torque-velocity scaling, and passive functions were defined for the different coupling equations, as well as the activation function. The Biodex System 4 Pro™ was used to determine the net joint torques at the shoulder for 20 participants in isometric, isokinetic, and passive tests. Data was processed and normalized to compare the relative shoulder strength of individuals. MATLAB's Curve Fitting Toolbox™ was used to find the curves or surfaces that best fit the experimental data for the MTG functions with different degrees of coupling. A completely general model, a female general model, a male general model, and 13 subject-specific models were fit for the three coupling methods. It was found that subject-specific models tended to fit higher-order curves and surfaces compared to the general models that contained averaged data.

The models were validated against experimental isokinetic torque data. It was determined that the male general model with position coupling resulted in the lowest error (6.4%), with the position coupling for the completely general model resulting in the next lowest error (8.0%). The female general model resulted in higher errors (average error of 19.9% $\pm$ 7.1%), with limited coupling showing the best results with an error of 11.6%. For subject-specific models, it was determined that the average error was the lowest for position and velocity coupling with an error of 22.8% and increasing with decreased coupling. The subject-specific models predicted the general torque trend well for most participants; however, the subject-specific models were highly dependent on the participant's consistent effort during data collection. The work demonstrated that subject-specific, completely general, female general, and male general MTG models can predict torque results that are dependent on multiple DOF of the shoulder. Future work should include the addition of a fatigue model and the bi-articular nature of the biceps brachii.

Acknowledgements

I would like to sincerely thank my supervisor, Prof. John McPhee for the opportunity to conduct this research and for the guidance and support he provided throughout this project.

I would like to thank all those who participated in and returned to my study, as without their assistance I would not have the experimental data needed to complete this project.

Finally, I would like to thank all the members of the Motion Research Group at the University of Waterloo for their suggestions and support over the past two years.

This research was funded by the Natural Sciences and Engineering Research Council of Canada and the University of Waterloo.

Table of Contents

List of Figures viii

List of Tables xi

List of Abbreviations xii

List of Symbols xiii

1 Introduction 1

1.1 Motivation and Goals . . . 1
1.2 Contributions . . . 2
1.3 Document Structure . . . 2

2 Background and Literature Review 4

2.1 Muscle-Force Models . . . 4
2.2 Muscle Torque Generator Models . . . 5
2.2.1 Overall Model . . . 5
2.2.2 Torque-Angle Scaling Functions . . . 6
2.2.3 Torque-Velocity Scaling Functions . . . 9
2.2.4 Passive Functions . . . 13
2.2.5 Activation Functions . . . 14
2.3 Summary . . . 16

3 Multi-Degree-of-Freedom Muscle Torque Generator Model **17**

3.1 Definition of Model Joint Torques and Angles 17

3.2 Coupling Equations 19

3.3 Muscle Torque Generator Function Equations 21

4 Shoulder Experiments **24**

4.1 Setup 24

4.1.1 System Used 24

4.1.2 Joint Alignment 24

4.2 Elevation Torque Data 25

4.2.1 Subjects 26

4.2.2 Isometric Test 26

4.2.3 Passive Test 26

4.3 Plane of Elevation Torque Data 27

4.3.1 Subjects 27

4.3.2 Isometric Test 27

4.3.3 Passive Test 28

4.4 Isokinetic Data 29

4.5 Data Processing 30

5 Multi-Degree-of-Freedom Muscle Torque Generator Model Fitting and Comparison **36**

5.1 Parameter Fitting 36

5.1.1 Methods 37

5.1.2 Fitting Results 40

5.2 Model Validation 47

5.2.1 General Models 49

5.2.2 Subject-Specific Models 60

6 Conclusion **65**

6.1 Research Summary 65

6.2 Limitations 66

6.3 Recommendations and Future Work 68

References **69**

APPENDICES **77**

A Additional Muscle Torque Generator Functions from the Literature **78**

B Muscle Torque Generator Model Parameters **80**

B.1 Completely General Model Parameters 80

B.2 General Female Model Parameters 83

B.3 General Male Model Parameters 91

List of Figures

2.1 A comparison of the normalized torque-angle scaling mathematical models evaluated by Haering *et al.* [24]. 8

2.2 A comparison of the normalized torque-velocity scaling functions modeled by King and Yeadon [38], Yeadon *et al.* [73], Anderson *et al.* [3], and McNally and McPhee [50]. 12

2.3 Comparison of the normalized passive hip torque results for hip extension to flexion for the models designed by Yoon and Mansour [74] and Anderson *et al.* [3]. 14

2.4 The normalized activation function used by McNally and McPhee [50] where the activation time was set to 0 seconds and deactivation time was set to 0.6 seconds. 15

3.1 Torque and angle definitions for shoulder plane of elevation and shoulder elevation. The coordinate system is defined for the right arm with the person facing towards positive X. 18

3.2 Visualization of ROM defined for the multi-DOF shoulder MTG model. The anterior and posterior directions are defined. 19

3.3 The sine and cosine relationship of a_1 and a_2, and the resultant torque direction α for the first activation approach. 23

4.1 Example of a participant setup when θ_1 is 0 deg and θ_2 is 85 deg for isometric testing in elevation 27

4.2 Example of a participant setup when θ_1 is 0 deg and θ_2 is 85 deg for the plane of elevation isometric testing. 28

4.3 Example of a participant setup when the Biodex axis is tilted 30 deg from the vertical. The participant was limited to 5 deg/s, resulting in a $\dot{\theta_1}$ of 2.5 deg/s and a $\dot{\theta_2}$ of 4.3 deg/s for the trial. 29

4.4 Example of a participant's isometric toque results for a 5s contraction. The highest average torque is found over 0.5s intervals to determine the isometric torque for the specific angle. 30

4.5 Example of regression used to create a maximal isokinetic dataset. 31

4.6 Box plot of each participant's normalized torque data (normalized by τ_{max}) used to identify outliers. The median is represented by the red bar, the upper and lower quartiles by the box, the maximum and minimum values excluding outliers by the dotted lines, and the outliers by the red crosses. . 33

4.7 Concentric activations for a given α for the completely general model, the female general model and the male general model. 35

4.8 Eccentric activations for a given α for the completely general model, the female general model and the male general model. 35

5.1 Example of a piecewise torque-velocity scaling function curve fit with an intercept constraint at 1 when $\dot{\theta_2} = 0$. The solid line in red represents a second-degree curve fit to the concentric data. The dashed red line represents the linear fit for the eccentric data. 39

5.2 Example of a surface fit used for the torque-angle scaling function. A 3,2-Surface was found to be the best fit for the experimental data. 39

5.3 Comparison of the completely general and female general model for the position-coupled torque-angle scaling function in elevation ($\tau_{\theta_2}(\theta_1, \theta_2)$). . . 43

5.4 Example of a 3-Curve fit for the torque-velocity scaling function in the plane of elevation ($\tau_{\omega_1}(\dot{\theta_1})$) for the female general model. 44

5.5 Comparison of the female general model and male general model for the torque-velocity scaling function in elevation ($\tau_{\omega_2}(\dot{\theta_2})$). 45

5.6 Comparison of the completely general model in plane of elevation and elevation for the coupled passive functions ($\tau_{p_1}(\theta_1, \theta_2)$ and $\tau_{p_2}(\theta_1, \theta_2)$). 46

5.7 Torque results of the completely general model for Method 1, 2, and 3 using the first activation method compared against experimental torque data averages across all participants. 51

5.8 Torque results of the female general model for Method 1, 2, and 3 using the first activation method compared against experimental torque data averages across all female participants. 52

5.9 Torque results of the male general model for Method 1, 2, and 3 using the first activation method compared against experimental torque data averages across all male participants. 53

5.10 Torque results of the completely general model for Method 1, 2, and 3 using the second activation method compared against experimental torque data averages across all participants. 56

5.11 Torque results of the female general model for Method 1, 2, and 3 using the second activation method compared against experimental torque data averages across all female participants. 57

5.12 Torque results of the male general model for Method 1, 2, and 3 using the second activation method compared against experimental torque data averages across all male participants. 58

5.13 Torque results of the subject-specific model of one participant using the first activation method for Methods 1, 2, and 3 compared against the experimental torque data of the participant. 62

5.14 Torque results of the subject-specific model of one participant using the second activation method for Methods 1, 2, and 3 compared against the experimental torque data of the participant. 64

List of Tables

3.1 Summary of Coupling Equations 21

5.1 Summary of Muscle Torque Generator Functions and the Number of Best Curves and Surfaces Fit 38

5.2 General Muscle Torque Generator Functions Fitting Results and Accuracy 42

5.3 Subject-Specific Muscle Torque Generator Functions Average Fitting Results and Accuracy 48

5.4 General Model Validation Results For Total Torque Using the First Activation Method A1 50

5.5 General Model Validation Results For Total Torque Using the Second Activation Method A2 55

5.6 Average Subject-Specific Model Validation Results For Total Torque Using the First Activation Method A1 60

5.7 Average Subject-Specific Model Validation Results For Total Torque Using the Second Activation Method A2 61

List of Abbreviations

DOF Degree of Freedom iii, 1–3, 5, 6, 16–20, 49, 59, 61, 63, 65, 67, 68, 73, 76, 84

EMG Electromyography 9, 67, 68

IQR Interquartile Range 32

ISB International Society of Biomechanics 17

MTG Muscle Torque Generator iii, 1–7, 13, 15–24, 28, 34, 36, 37, 40, 47, 49, 59–61, 63, 65–67, 73, 76, 84

MVC Maximum Voluntary Contraction 26, 27, 29, 30, 41, 47, 54, 59, 60, 63, 66, 68

RMSE Root Mean Square Error 43, 49, 55, 59

RMSPE Root Mean Square Percentage Error 37, 40, 41, 43, 45–47, 49, 54, 55, 59

ROM Range of Motion 7, 13, 14, 16, 18–21, 26, 28, 45, 67, 69

SJC Shoulder Joint Center 24, 25

List of Symbols

E The eccentric torque relative to concentric torque, used in the model by Anderson *et al.* 10

ROM The range of motion for a specific joint 7

S The ratio of the change in torque and the change in velocity between the eccentric and concentric phases 11

a_1 The muscle activation term for the plane of elevation torques 22, 23, 32, 59

a_2 The muscle activation term for the elevation torques 22, 23, 32, 59

α_{max} The maximum activation level, often assumed to be 1 10

α_{min} The minimum activation level in the eccentric phase 10

α The direction of the resultant torque 18, 22, 23, 25, 32, 34, 35, 49, 59

a The muscle activation term, often between 0 and 1 6, 14, 15

Δ^P The term used to scale the passive curve used by Millard *et al* 6

Γ The shaping factor for the torque-velocity curve 11

λ^A The fitting parameter for the torque-angle curve used by Millard *et al.* 6

λ^P The fitting parameter for the passive curve used by Millard *et al.* 6

λ^V The fitting parameter for the torque-velocity curve used by Millard *et al.* 6

ω_1 The inflection point on the curve described by Equation 2.7 10

ω_{50} The angular velocity at which the torque is 50% of the maximum isometric torque, used in the model by Anderson *et al.* 10

ω_{75} The angular velocity at which the torque is 75% of the maximum isometric torque, used in the model by Anderson *et al.* 10

ω_c The vertical asymptote of the Hill hyperbola 10

ω_{max} The angular velocity where the torque-velocity scaling curve reaches zero torque 10

ω_r The ascent range of α_{min} to α_{max} 10

ω The joint angular velocity for an arbitrary single DOF MTG 6

s^A The term used to scale the torque-angle curve used by Millard *et al.* 6

s^τ The term used to scale the maximum isometric torque used by Millard *et al.* 6

s^V The term used to scale the torque-velocity scaling curve used by Millard *et al.* 6

t' The time from disengagement of the muscle torque generator 15

t_{act} The activation time constant 15

τ_1 The torque responsible for shoulder plane of elevation and in the direction of θ_1 18–20, 22, 23, 31, 32, 36, 37, 40

τ_2 The torque responsible for shoulder elevation and in the direction of θ_2 18–20, 22, 23, 31, 32, 36, 37, 41

τ_{act} The scalar activation torque of an MTG (lies between τ_{min} and τ_{max}) 5–7, 22, 32

τ_θ The torque-angle scaling function of an MTG 6

τ_{ecc} The ratio between the maximum eccentric torque and maximum isometric torque 10

τ_{max} The maximum allowed isometric torque for an MTG 5, 7, 14, 22, 23, 32

τ_{min} The minimum allowed isometric torque for an MTG 5, 14

τ_p The passive torque function of an MTG 6

τ_ω The torque-velocity scaling function of an MTG 6

τ The resultant torque in the direction of α 18, 22

θ^+ The maximum angle of a joint's range of motion 13, 14

θ^- The minimum angle of a joint's range of motion 14

θ_0 The angle where torque production is optimal 7

θ_1 The angle describing the plane of elevation of the humerus relative to the thorax 17–20, 25–29, 37, 41, 49

θ_2 The angle describing the elevation of the humerus relative to the thorax 17–20, 25–28, 37, 41, 45, 46, 49

θ_{max} The largest angle where torque production reaches zero 7

θ_{min} The smallest angle where torque production reaches zero 7

θ_{off} The angle offset from the joint's maximum angle, used in Yoon and Mansour's passive model 13

$\dot{\theta_1}$ The angular velocity describing the rate of change of the plane of elevation of the humerus relative to the thorax 19, 29, 31, 44, 49

$\dot{\theta_2}$ The angular velocity describing the rate of change of elevation of the humerus relative to the thorax 29, 31, 39, 44, 49

θ The joint angle for an arbitrary single DOF MTG 6

t The time from activation for the muscle torque generator 15

Chapter 1

Introduction

Forward dynamic musculoskeletal simulations allow for the safe study of complex motions. Applications include optimizing athlete performance [7, 33, 50], movement science [62], design of assistive devices [64, 52], and rehabilitation planning [36]. To create a human model for simulations, a reasonable representation of muscles is required, and commonly muscle-force models based on the Hill-type muscle model are applied [28]. However, these muscle-force models have some drawbacks. One drawback includes the need to define muscle geometry such as the insertion point, wrapping, and the muscle moment arm [11, 60]. There is also the muscle redundancy issue, in which there are more muscles at a joint than DOF, and therefore optimization is normally required to solve for a motion [12]. Finally, these muscle-force models require parameters that can be difficult to fit [31]. One solution to the mentioned drawbacks is to use a Muscle Torque Generator (MTG) as it reduces the complexity of muscle-force models to a single torque at the joint, all while maintaining the position and velocity dependencies of muscles [31]. The simplicity of MTGs allows for faster forward dynamic simulations of complex motions.

1.1 Motivation and Goals

While MTGs help reduce the complexity of muscle-force models, they currently can only be used for single DOF joints, and additional MTGs are often added to represent joints with more DOF [46]. Currently, there is no MTG that can be used for three-dimensional joint motion that accounts for coupling between the DOF [48]. Therefore, the goal of this work is to develop, for the first time, an MTG model that accounts for the coupling between 2 DOF for the shoulder joint. The shoulder joint, also known as the glenohumeral

joint, was selected as it has 3 DOF and it has torques generated from multiple muscles with different lines of action [66, 47]. The model aims to simplify the complexity of the shoulder joint to allow for simpler and faster simulations. In the first phase of this thesis, three different forms of the 2 DOF MTG model for the shoulder joint were designed with different degrees of coupling between DOF to allow for a comparison. The different scaling functions for the MTGs were also defined. In the next phase, biomechanical torque data was gathered to identify the parameters in the designed models. Finally, in the third phase, the subject-specific and general models were fit to the experimental data for the three different coupling methods. The ability to predict joint torque was evaluated against experimental torque data for the subject-specific, completely general, female general, and male general models, leading to a comparison of degrees of coupling and model accuracy.

1.2 Contributions

The contributions of this work include:

- Development of subject-specific and general multi-DOF MTGs as a function of two joint angles and angular velocities for the first time.
- Gathered experimental torque data in terms of two joint angles and two joint angular velocities at the shoulder, supporting the development of the MTG model.
- Compared how the degree of coupling between the angles and angular velocities of the shoulder affected the accuracy of the resultant MTG models.

1.3 Document Structure

The following describes the organization of the document:

- Chapter 1 provides an introduction to the work presented in this thesis, outlining the motivation and goals as well as the project contributions.
- Chapter 2 provides the background on muscle-force models as well as current MTG models, their structure, and the functions that are used to formulate the MTG models.

- Chapter 3 outlines the multi-DOF MTG model that was developed for the shoulder. The angles and torques are defined for the model as well as the coupling equations and scaling functions used.
- Chapter 4 describes the collection and processing of the biomechanical data collected for the shoulder. The first sections highlight the collection of elevation and the plane of elevation isometric and passive torques, followed by the isokinetic torques obtained. The data processing steps for the different data types are then described.
- Chapter 5 details the multi-DOF model fitting and compares the accuracy of the different coupling equations. The first section outlines the different parameter fitting methods used, followed by the results of fitting the different coupling equations and subject-specific and general models. The accuracy of the models is then evaluated from comparisons against experimental data.
- Chapter 6 concludes the research done in this thesis by summarizing the work. Limitations of the model and recommendations for future work are also discussed.

Chapter 2

Background and Literature Review

The literature has been reviewed to understand the principles behind MTGs and their applications. MTG models offer an alternative to muscle-force models, so first a short review of muscle-force models including the underlying muscle principles and their limitations is presented. Next, a detailed review of the current MTG models and the different functions used to represent human joint torque is outlined. Finally, a summary of the different approaches to model MTGs is provided.

2.1 Muscle-Force Models

As previously mentioned in Chapter 1, a reasonable representation of joint actuation is required to model a human in forward dynamic simulations, with common models used being muscle-force models. Often, muscles and tendons are represented as massless cables with insertion points and muscle wrapping around the skeleton [14, 59]. Typically, these models are based on the model by Hill [28] and consist of a contractile element as well as a series elastic and parallel elastic element [70, 75]. The force the muscle produces depends on several factors, with some of the main factors being the muscle length, which is described by force-length curves [22], and the muscle lengthening rate, described by force-velocity curves [28], as well as the muscle pennation angle and the maximum isometric force the muscle can produce [31]. In the mono-articular case, these muscles span one joint and cause tension to act on the tendon, which in turn causes a force to act on the bone, with the resulting joint torque depending on the moment arm [31, 60].

While muscle-force models are useful for simulations where individual muscle forces or bone-on-bone contact forces are needed, they can introduce additional complexities in

situations where this is not required [51]. The need to define muscle geometry such as the insertion point, wrapping, and the muscle moment arm for the models leads to parameters that are difficult to obtain from living humans [11, 60]. There is also more than one muscle crossing a joint, which causes the muscle redundancy issue, and therefore optimization is normally required to solve for a motion [12]. MTGs offer a solution to the problems mentioned above and will be reviewed in the following section.

2.2 Muscle Torque Generator Models

An MTG is a model that reduces the complexity of muscle-force models to a single torque at the joint, all while maintaining the position and velocity dependencies of muscle forces [31]. To date, there have been several different approaches to the overall MTG model. However, typically the models are functional equations containing a torque-angle scaling function, which represents the length-dependent properties of muscles, a torque-velocity scaling function, which represents the muscle lengthening dependent properties, a passive function which considers forces from viscoelastic elements of the muscle, and finally the activation function, which gives activation torque [31]. The application of the MTG model can vary the functions used in the overall model and often dynamometry is used to determine parameters for the specific joint being evaluated [3, 6, 20, 23, 38, 73]. The specific joint being modeled, even if it has more than one DOF, is modeled using a single DOF MTG per DOF [46]. The following sections outline different approaches to the overall model, followed by the different modeling approaches for the functional components.

2.2.1 Overall Model

In the work done by Inkol *et al.* [31], the standard form of an MTG is defined using the following equation:

$$\tau(\tau_{act}, \theta, \omega) = \tau_{act} \cdot \tau_{\omega}(\omega) \cdot \tau_{\theta}(\theta) + \tau_{p}(\theta, \omega) \tag{2.1}$$

Equation 2.1 operates under the assumption of tendon rigidity. The scalar activation torque, τ_{act}, lies between τ_{min}, the minimum allowed isometric torque, and τ_{max}, the maximum allowed isometric torque. The minimum isometric torque, τ_{min}, can be defined in either the positive direction or the negative, depending on the simulation being conducted. For example, in the work of McNally and McPhee [50], the minimum isometric torque was

set to zero, and each joint was actuated by two MTGs to provide torque in both directions, while in the work of Jansen and McPhee [33], only one MTG was applied per joint and the minimum isometric torque was set to be the maximum isometric torque in the opposite direction. τ_θ and τ_ω are the torque-angle and torque-velocity scaling functions, respectively. τ_θ depends on θ, which is the angle of the single DOF joint, and τ_ω depends on ω, the rate of change of θ. τ_p represents the passive torques that are caused by the passive viscoelastic elements in muscles.

Extending the work done by Forrester *et al.* [20], an alternative to the above equation has been proposed by Millard *et al.* [51] and can be seen in Equation 2.2.

$$\begin{aligned}\tau(a,\theta,\omega) = s^\tau \tau_{max}(a \cdot \tau_\theta(\theta, s^A, \lambda^A) \cdot \tau_\omega(\omega, s^V, \lambda^V) \\ +\tau_p(\theta, \Delta^P, \lambda^P)(1 - \beta^P E \frac{\omega}{s^v \omega^M_{max}}))\end{aligned} \tag{2.2}$$

The torque-angle scaling, torque-velocity scaling, and passive torque functions, similar to the approach used in 2.1, are defined using τ_θ, τ_ω, and τ_p. However, unlike the previous MTG equation that uses different methods of scaling functions, this model employs 5^{th}-order Bezier curves to define the functions. Muscle activation, a term that can be considered using the activation torque τ_{act}, is represented using a. An additional non-linear damping term was added to the passive torque function in order to reduce vibrations. Fitting parameters, λ^A, λ^V, and λ^P, and scaling parameters, s^A, s^V, and Δ^P, are used for the torque-angle scaling, torque-velocity scaling, and passive torque functions, respectively. Finally, the term s^τ is used to scale the maximum isometric torque.

While the author of this thesis has seen the above method applied less frequently, a benefit is that most parameter terms have a physical meaning; for example, increasing the scaling term s^A effectively increases the optimal fiber length of muscles. Millard *et al.* used quadratic programming to systematically fit these parameters to different dynamometer data sources.

2.2.2 Torque-Angle Scaling Functions

The torque-angle scaling function scales the maximum isometric torque such that the length-dependent properties of muscles are incorporated. Often, this is done using polynomial functions as the degree of the polynomial can be easily adjusted, and parameter identification is flexible [6, 24, 23, 33]. However, the implementation often depends on the application. Different variations of the torque-angle scaling function are presented below.

Kulig *et al.* [40] conducted work to determine human strength curves, which are curves that outline the torque-angle relationship of a joint. The authors found that a similar trend could be seen between the torque-angle curve of a joint and the force-length curve of muscles. In a typical force-length strength curve, a peak in muscle strength is achieved when the sarcomere length is optimal, and zero force is seen at the smallest and longest lengths [22]. Previous mathematical models that aim to model the force-length curves of muscles can therefore be used as inspiration for the torque-angle scaling function. The force-length curve has been previously modeled using a normal [4], quadratic [9], and sine-exponential curve [26] as well as a spline interpolation [44]. While there is no consensus on which model should be used for the force-length curve, Kulig *et al.* discuss that the strength dependency can have one of three general behaviours: an ascending behaviour, a descending behaviour, and an ascending-descending behaviour [40].

Anderson *et al.* [3] considered the three behaviours discussed by Kulig *et al.* [40] and chose to model the torque-angle scaling as a sinusoidal function as it captures all behaviours mentioned. The model below in Equation 2.3 was used to represent the torque-angle scaling for applications to the lower limb. It can be noted that this equation contains the maximum isometric torque τ_{max}. While some researchers choose to incorporate the maximum isometric torque in the τ_{act} term of models, others choose to add it to the torque-angle scaling function. Often, it depends on the style of activation function that is used, as the τ_{max} term only needs to be applied once in the MTG.

$$\tau_\theta(\theta) = \tau_{max} \cdot cos\left(\pi \frac{\theta - \theta_0}{\theta_{max} - \theta_{min}}\right) \tag{2.3}$$

In Equation 2.3, θ_0 is the angle where torque production is optimal, and θ_{max} and θ_{min} are the maximum and minimum angles where torque production is zero. The authors used the torque-angle scaling together with a torque-velocity scaling function to determine the active torque of lower limb muscles, gathering experimental data using a dynamometer and finding that they were able to predict knee extension torque with an R^2 value as high as 0.942.

Haering *et al.* [23] studied the effect that different torque-angle scaling functions had on predicting torque accuracy for the elbow. Five different mathematical models were compared: a normal, cosine, quadratic, cubic, and sine-exponential function, which can be seen in Equations A.1, A.2, A.3, A.4, and A.5, respectively. The key terms in these equations are θ_0 and ROM, with ROM being the Range of Motion (ROM) of the joint specified. However, ROM can be defined as the difference between the maximum and minimum angle (θ_{max} - θ_{min}) and therefore Equation A.2 is equivalent to Equation 2.3.

The authors noted that previous to their work, there was no consensus on which style of mathematical model was best to determine torque-angle scaling for the elbow. They determined that the cosine, quadratic, and cubic models performed better than the normal and sine-exponential models, with the quadratic providing the best fit for a wide selection of participants. A comparison of the different mathematical models evaluated by Haering *et al.* [24] is depicted in Figure 2.1.

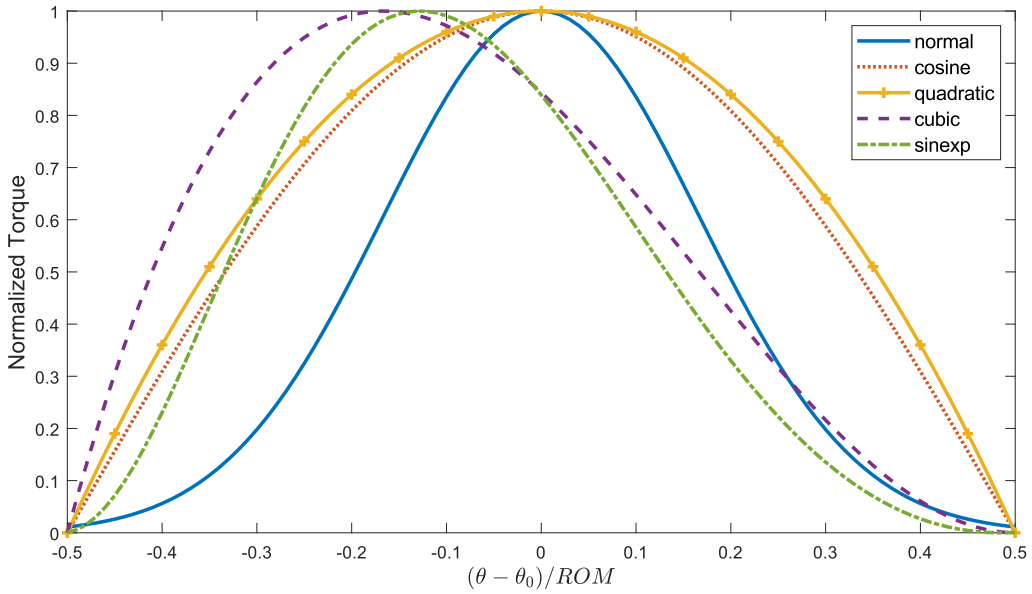

Figure 2.1: A comparison of the normalized torque-angle scaling mathematical models evaluated by Haering *et al.* [24].

In the work of Brown and McPhee [6], different polynomial functions were used to model the elbow, wrist, and shoulder of a wheelchair basketball athlete. It was determined that a second-order polynomial provided the best fit for the elbow and wrist; however, a 4^{th}-order polynomial provided the best fit for the shoulder. The second-order polynomial was based on previous work [37, 20], and curve-fitting was used to determine the parameters. Equation 2.4 shows the polynomial torque-angle scaling function used for the shoulder.

$$\tau_\theta(\theta) = a\theta^4 + b\theta^3 + c\theta^2 + d\theta + e \tag{2.4}$$

To model Olympic track cycling standing starts, Jansen and McPhee [33] used the cosine function outlined in Equation 2.3 to similarly capture the muscle behaviours as in

Anderson *et al.* [3]. As the lower limbs were the joints in question for the model, parameters were adopted from [3] and [39].

In the work of McNally and McPhee [50], a biomechanical model of the golf swing was modeled. Due to the ballistic motion of the golf swing, the authors chose not to include a torque-angle scaling function and instead focused on the torque-velocity scaling function, which will be discussed in the next section.

2.2.3 Torque-Velocity Scaling Functions

The torque-velocity scaling function scales the maximum isometric torque production such that the lengthening properties of muscles are considered. Typically, a piecewise function is used to capture the nature of concentric and eccentric motions [3, 73, 50], with a hyperbolic curve being a common component [3, 23, 73].

During a concentric motion, an increase in the speed of muscle shortening causes the muscle force to decrease in a hyperbolic nature [28]. However, in the eccentric phase, it has been found that maximum muscle force will increase to a value of 1.5 times the isometric force, with a plateau at higher speeds [25]. King and Yeadon [38] created a model that captured the double hyperbolic shape mentioned and applied the model in Equation 2.5. This model employed the positive parameters a, b, c, d, p, and q, which were determined by minimizing the squared difference between experimental values and the model results. The authors found the fit of the function to be sufficient for the data collected; however, when extrapolating beyond what was measured, there was a degradation in performance.

$$\tau_\omega(\omega) = \frac{a + be^{p\omega}}{(1 + ce^{p\omega})(1 + de^{q\omega})} \tag{2.5}$$

In the work of Yeadon *et al.* [73], the authors modeled the maximum joint torque over a range of angular velocities. However, the authors discuss that in studies of human skeletal muscle, the 1.5 increase of eccentric force over isometric force is rarely achieved, with the force increasing minimally over the maximum isometric force [68]. With electrical stimulation, this eccentric torque can be increased beyond the isometric torque by greater than 20% [69], and when measuring eccentric loading without stimulation, it was found that Electromyography (EMG) activity did not change over eccentric velocities, leading to the theory that lower forces are achieved during eccentric contractions as a means of injury protection [67]. Yeadon *et al.* therefore created a model that accounted for the activation profile of eccentric motions.

Yeadon *et al.* defined two models, a four parameter function and a seven parameter function, which consist of the four parameter function combined with a three parameter activation function that defines the activation profile. Equation 2.6 gives the four parameter concentric and eccentric torque relationship, where τ_{ecc} is the ratio between the maximum eccentric torque and maximum isometric torque, ω_{max} is the angular velocity where the curve reaches a torque of zero, and ω_c is the vertical asymptote of the Hill hyperbola.

$$\tau_\omega(\omega) = \begin{cases} \frac{C}{(\omega_c+\omega)} - \tau_c & \omega \geq 0 \\ \\ \frac{E}{(\omega_e-\omega)} + \tau_{ecc} & \omega \leq 0 \end{cases} \tag{2.6}$$

In the above equation, $\tau_c = \frac{\tau_{max}\omega_c}{\omega_{max}}$, $C = \tau_c(\omega_{max} + \omega_c)$, $\omega_e = \frac{(\tau_{ecc}-\tau_{max})}{4.3\tau_{max}} \frac{\omega_{max}\omega_c}{(\omega_{max}+\omega_c)}$ and $E = -(\tau_{ecc} - \tau_{max})\omega_e$.

Equation 2.7 is the three parameter activation function that, when multiplied by the four parameter function, forms the seven parameter model. The parameter α_{max} is the maximum activation level, which is often assumed to be 1, and α_{min} is the minimum activation level in the eccentric phase. The inflection point on the curve described by Equation 2.7 is ω_1, and finally, ω_r is the ascent range of α_{min} to α_{max}.

$$\alpha(\omega) = \alpha_{min} + \frac{\alpha_{max} - \alpha_{min}}{\left[1 + e^{\frac{\omega-\omega_1}{\omega_r}}\right]} \tag{2.7}$$

Yeadon *et al.* found that this seven parameter function allowed for both maximal and submaximal activities to be modeled. However, the authors set τ_{ecc} to a constant value of 1.5 and found some simulation results to be unrealistic. The model has been found useful for sports simulations [31], with it being applied in Brown and McPhee's [6] forward dynamic simulation of manual wheelchair propulsion.

Anderson *et al.* [3] based their concentric torque relationship on Hill's hyperbolic function [28]. The concentric torque relation can be seen when the angular velocity is greater than zero in Equation 2.8. In this equation, ω_{75} and ω_{50} define the shape of the parabola and correspond to the angular velocity at which the torque is 75% and 50% of the maximum isometric torque, respectively. In order to consider the eccentric torque, the authors scaled the concentric torques linearly with velocities based on the work by Dudley *et al.* [16], where the relationship of eccentric to concentric torque in the knee was shown to increase with speed. The parameter E was added to help define the eccentric to concentric torque relation. The model developed here has been applied in forward dynamic

simulations, with Jansen and McPhee [33] applying it to a predictive simulation of Olympic track cycling starts due to Anderson's specific application to the lower limbs.

$$\tau_\omega(\omega) = \begin{cases} \frac{2\omega_{75}\omega_{50}+\omega(\omega_{50}-3\omega_{75})}{2\omega_{75}\omega_{50}+\omega(2\omega_{50}-4\omega_{75})} & \omega \geq 0 \\ \\ \frac{2\omega_{75}\omega_{50}-\omega(\omega_{50}-3\omega_{75})}{2\omega_{75}\omega_{50}-\omega(2\omega_{50}-4\omega_{75})}(1-E\omega) & \omega \leq 0 \end{cases} \tag{2.8}$$

Haering *et al.* [23] created and compared a new model with the model developed by Anderson *et al.* to address the derivative discontinuity in Anderson's model (see Figure 2.2) to avoid jumps in continuity and issues when fitting the curves to experimental data. The authors designed a new power-based model, which is a polynomial function that considers the concentric velocity where power is maximal, basing the addition of the velocity term on previous work that found it to be correlated to muscle composition [21, 58]. The maximum power velocity is used as an inflection point in the concentric phase of the torque-angle scaling function. The authors found that the new power-based model fit concentric data better than Anderson's model, but was worse at fitting eccentric data due to the constraint that ensured continuity between the eccentric and concentric phases.

Sprigings and Neal [61] and MacKenzie and Sprigings [46] used torque-velocity scaling without torque-angle scaling to adjust the torques after the muscle activation had already been considered in their forward dynamic model of the golf swing. The scaling used was originally applied for high and long jumps by Alexander [1], and an interesting feature of this model is the lack of a piecewise function for concentric and eccentric motions due to the motion studied not including a negative angular velocity.

$$\tau_\omega(\omega) = \frac{(\omega_{max}-\omega)}{(\omega_{max}+\Gamma\omega)} \tag{2.9}$$

The parameter Γ is the shaping factor for the torque-velocity curve. The work done by Alexander, Sprigings and Neal, and by MacKenzie and Sprigings was extended by McNally and McPhee [50] by incorporating the work done by Van Soest, who outlined a general form for the eccentric relationship [65]. A piecewise function was used to represent the concentric and eccentric velocities as seen in Equation 2.10; McNally and McPhee extended the motion of the golf swing such that negative angular velocities were considered. The term S is the ratio of the change in torque and the change in velocity between the eccentric and concentric phases.

$$\tau_\omega(\omega) = \begin{cases} \frac{(\omega_{max}-\omega)}{(\omega_{max}+\Gamma\omega)} & \omega \geq 0 \\ \frac{(1-\tau_{ecc})\omega_{max}+S\omega\tau_{ecc}(\Gamma+1)}{(1-\tau_{ecc})\omega_{max}+S\omega(\Gamma+1)} & \omega \leq 0 \end{cases} \tag{2.10}$$

As previously mentioned, this model did not scale using a torque-angle function. However, a passive function was used, which will be covered in the next section.

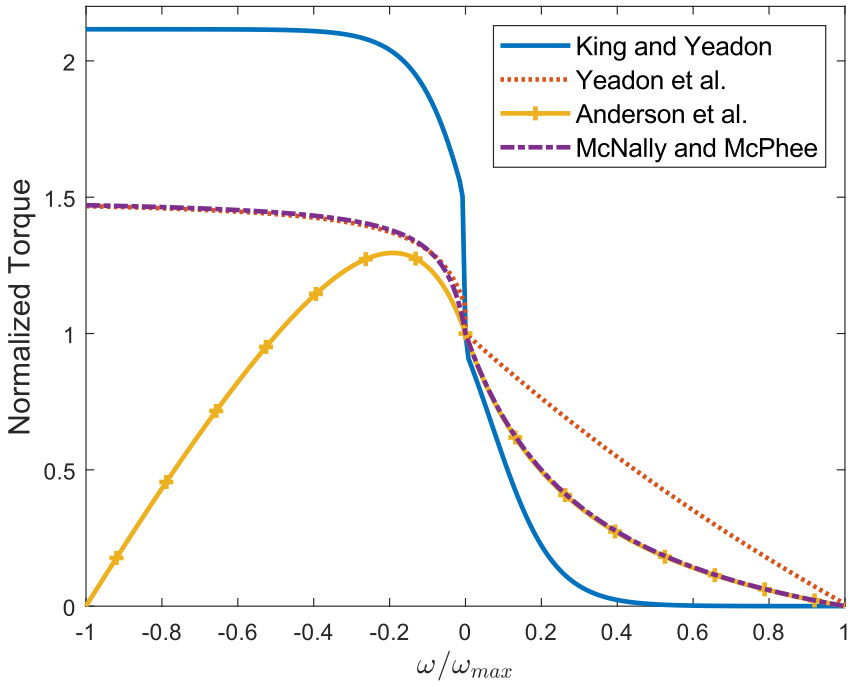

Figure 2.2: A comparison of the normalized torque-velocity scaling functions modeled by King and Yeadon [38], Yeadon *et al.* [73], Anderson *et al.* [3], and McNally and McPhee [50].

Figure 2.2 shows a normalized comparison of the double hyperbolic function by King and Yeadon, the piecewise four parameter function by Yeadon *et al.*, the piecewise function by Anderson *et al.*, and the piecewise function by McNally and McPhee. King and Yeadon obtained parameters from the force-velocity data of Edman [17] who studied the force-velocity relationship of frog muscles. Parameters for the function by Yeadon *et al.* were obtained from knee extension trials for a single subject, and parameters from Anderson *et*

al. were obtained from knee flexion trials for a single subject. McNally and McPhee used parameters matching the work done by Van Soest [64].

2.2.4 Passive Functions

The passive function allows for torques contributed by components in parallel with the contractile elements of muscle to be considered. These include structures such as tendons, ligaments and muscle tissues such as the epimysium and perimysium [3, 31]. In the literature, there are two main forms presented: a double-exponential form [3, 29, 57, 72] and a linear spring-damper form [37, 63].

King and Yeadon [38] modeled passive torque as a linear torsional spring, with a stiffness based on the elastic component of the muscle and tendon in the vasti muscles [32]. This method was later applied in the work by King *et al.* for the evaluation of MTG models for jumping [37].

Yoon and Mansour [74] used a double exponential function that helped to simulate the ROM of the joint. Equation 2.11 was applied twice, once for hip flexion and a second time for hip extension, with parameters k_1, k_2, k_3, and k_4 being modified for the motion. The maximum angle for the joint's range of motion, θ^+, and θ_{off}, the angle offset from the joint's maximum angle, were also modified for flexion versus extension. While this model performed well, the θ_{off} term can complicate the application to joints other than the joint studied.

$$\tau_p(\theta) = k_1(e^{k_2(\theta-\theta^+)} - 1) + k_3(e^{k_4(\theta-\theta_{off})} - 1) \tag{2.11}$$

Hoang *et al.* [29] applied a similar double exponential function at the ankle, considering the sum of torque in both plantar flexion and dorsiflexion. Riener and Edrich [57] also applied a similar double exponential function. However, biarticular muscles that cross two joints were considered in their model, with the angle of the adjacent joint factoring into the model equations.

Anderson *et al.* [3] based their work on the double exponential models previously mentioned [74, 29], and presented a slightly simpler model, seen in Equation 2.12. In this equation, the ROM is enforced by the two terms and the passive equation itself is independent of the muscle activation.

$$\tau_p(\theta) = k_1 e^{k_2\theta} + k_3 e^{k_4\theta} \tag{2.12}$$

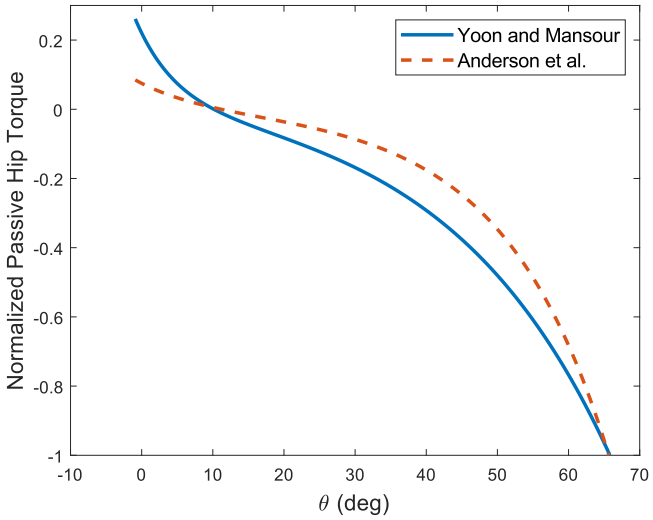

Figure 2.3: Comparison of the normalized passive hip torque results for hip extension to flexion for the models designed by Yoon and Mansour [74] and Anderson *et al.* [3].

Figure 2.3 compares the normalized passive hip torque results for hip extension to flexion for the models designed by Yoon and Mansour and Anderson *et al.* The model parameters were determined from two different participants that completed the motion.

Yamaguchi [72] uses the terms θ^+ and θ^- to define the feasible ROM in their double exponential passive function (Equation 2.13) which is easily adapted to other joints due to the parameter's physical meaning. A viscous damping term was also added with a recommend linear damping coefficient of $c = 0.1Nm \cdot rad^{-1}$.

$$\tau_p(\theta, \omega) = k_1 e^{-k_2(\theta - \theta^-)} - k_3 e^{-k_4(\theta^+ - \theta)} - c\omega \tag{2.13}$$

Yamaguchi's equation was later applied to the model of the golf swing used by McNally and McPhee [50].

2.2.5 Activation Functions

The activation function aims to capture the activation of muscles and provides a torque between the minimum isometric torque τ_{min} and the maximum isometric torque τ_{max}. Often, two main strategies are applied. The first strategy employs a function to capture the

activation dynamics of the model [46, 50, 73], and the second uses an activation parameter, a, that is often between 0 and 1 to scale the isometric torque depending on the muscle activation, or relative muscle effort [6, 33, 51]. The latter method is usually applied to an optimal control problem.

MacKenzie and Sprigings [46] used an activation curve to take into account the muscle activation and deactivation times for their model of the golf swing. In Equation 2.14, t and t' are the time it takes for the MTG to activate and de-activate, and t_{act} is the activation time constant. One thing to note about this equation is that the activation always leads to maximum muscle torque when the MTG is activated, and the muscle activation cannot be controlled further, making this equation more applicable to sports applications. McNally and McPhee [50] extended this equation by adding an exponential that acts to smooth the transition between activation and deactivation. Figure 2.4 shows the normalized activation function used by McNally and McPhee where the activation time was set to 0 seconds and deactivation time was set to 0.6 seconds.

$$\tau_a = \tau_{max}\left(1 - e^{\frac{-t}{t_{act}}}\right) - \tau_{max}\left(1 - e^{\frac{-t'}{t_{act}}}\right) \tag{2.14}$$

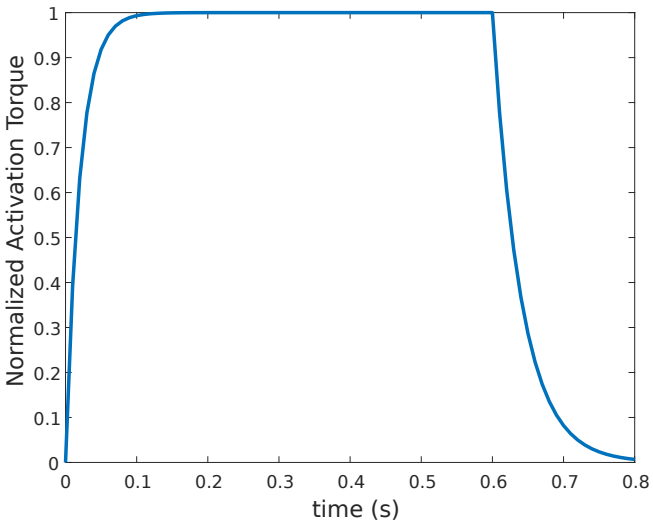

Figure 2.4: The normalized activation function used by McNally and McPhee [50] where the activation time was set to 0 seconds and deactivation time was set to 0.6 seconds.

Millard *et al.* [51], Brown and McPhee [6], and Jansen and McPhee [33] applied an activation term, a, to directly solve for the activation torque. This allows for torques less

than or equivalent to the maximum isometric torque. Jansen and McPhee specifically used an activation term of -1 to 1 to simulate the difference between muscles causing flexion and extension. In recent works by Jiang *et al.* [34], a similar activation term has been applied to their work of synthesising realistic human motion, where they are using novel machine learning techniques to solve for torque limits.

2.3 Summary

In summary, there are many methods previously used to develop an MTG for a single DOF joint. Dynamometry has been used to provide experimental data to fit the functions that define an MTG [3, 6, 20, 23, 38, 73]. However, there has not been a consensus on which style of functions to use. For torque-angle scaling, polynomial functions provide a simple approach, particularly for parameter fitting [6, 23]. In terms of torque-velocity scaling functions, a piecewise style function provides a better fit for both concentric and eccentric motions compared to a power-based model [23]. Passive torques are often minimal, except when outside an individual's ROM, which is then commonly represented by a double exponential function [3, 29, 57, 72]. Finally, the activation function tends to vary depending on the application, but for most forward dynamic simulations, an activation level that is controlled is applicable [6, 33, 51].

There are some general limitations to the MTG. These include the fact that bone-on-bone contact forces cannot be modeled using an MTG [51] and that antagonist co-contractions are not individually accounted for in the model [20]. One large limitation is the fact that an MTG can currently only be applied to single DOF joints, which often results in forward dynamic simulations being restricted to planar motions [19, 34, 18]. A previous approach applied two single DOF MTGs operating in horizontal and vertical directions and scaled them using a torque ratio term [49]. However, this approach does not consider the impact of the coupling between the two DOF of the joint, and to date there is no single MTG that is capable of providing torque for a three-dimensional motion [48]. Therefore, there is an opportunity to improve the MTG such that the coupling between two joint angles is considered in order to design an MTG for multi-DOF motion.

Chapter 3

Multi-Degree-of-Freedom Muscle Torque Generator Model

The definitions for the multi-DOF MTG are outlined in this chapter. Different coupling equations are presented to evaluate the effect that the degree of coupling has on the model. Finally, equations for the torque-angle and torque-velocity scaling functions as well as the passive and activation functions are outlined.

3.1 Definition of Model Joint Torques and Angles

The multi-DOF MTG model aims to capture the coupling between two major motions of the shoulder: shoulder plane of elevation, and shoulder elevation as defined according to the International Society of Biomechanics (ISB) [71]. Two angles were defined to describe these two motions. The first angle, θ_1, is defined as the angle of the plane of elevation of the humerus relative to the thorax. The second angle, θ_2, is defined as the angle of elevation of the humerus relative to the thorax (measured from -Y). Figure 3.1 depicts the coordinate system and angle definitions for the model. The coordinate system is defined using the ISB standards and is for the right arm with the person facing towards positive X.

Clinically, shoulder plane of elevation is defined as horizontal adduction when the humerus moves horizontally across and towards the chest and is defined as horizontal abduction when it moves horizontally away from the chest [53]. Shoulder elevation is clinically defined as abduction when the plane of elevation, θ_1, is 0 degrees and forward flexion when the plane of elevation is 90 degrees [71].

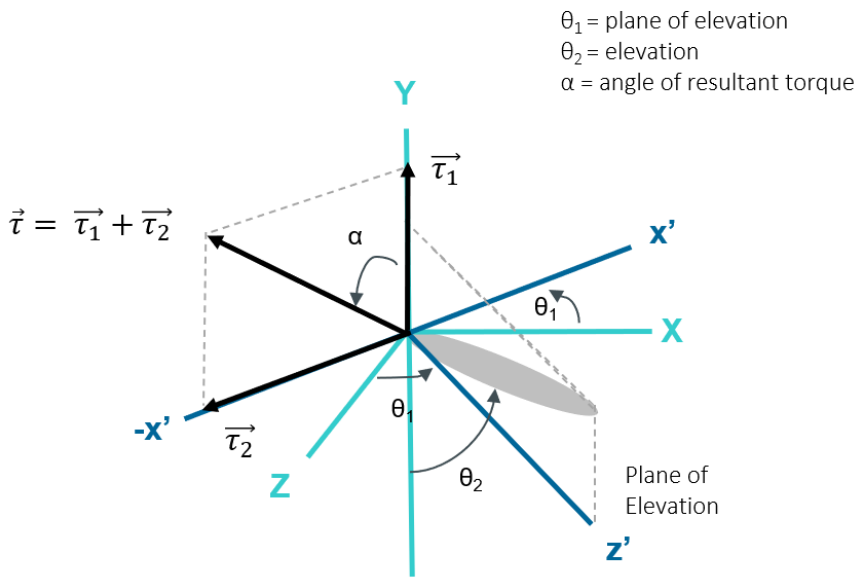

Figure 3.1: Torque and angle definitions for shoulder plane of elevation and shoulder elevation. The coordinate system is defined for the right arm with the person facing towards positive X.

To fully describe the model, one torque was defined per DOF. The first torque, τ_1, is the torque responsible for shoulder plane of elevation and is about Y in the direction of the first DOF (θ_1). The second torque, τ_2, is the torque responsible for elevation and is about -x' in the direction of the second DOF (θ_2). Each of these torques are individually determined by considering the coupling between the two DOF. The resultant torque, τ, is in the direction of α, which is defined in Figure 3.1.

The shoulder joint has a large ROM [66], ranging from 0 to 140 degrees in horizontal adduction and 0 to 167 degrees in forward flexion on average [54]. In order to reduce the ROM for the model to simplify the data collection process, the model use case was defined to be for lifting and reaching motions. Therefore, θ_1 was defined to be between 0 and 120 degrees and θ_2 between 60 and 160 degrees. This ensures that the joint angles are within the normal shoulder ROM, while removing the lower ranges of elevation which aren't as commonly used for lifting motions. Figure 3.2 shows a visualization of the ROM defined for the multi-DOF shoulder MTG.

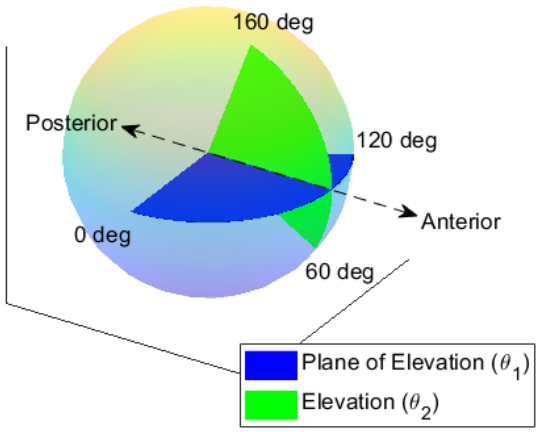

Figure 3.2: Visualization of ROM defined for the multi-DOF shoulder MTG model. The anterior and posterior directions are defined.

3.2 Coupling Equations

To develop the MTG forms for τ_1 and τ_2, the standard single DOF MTG equation seen in Equation 2.1 can be used as a template. One of the goals of this work is to determine the impact that different degrees of coupling between the two DOF has on model accuracy. To do this, models were developed that show limited coupling between the DOF, position coupling (such that the torque-scaling function is dependent on two DOF), and position and velocity coupling (where both the torque-angle and torque-velocity scaling are dependent on the two DOF).

First, equations for τ_1 and τ_2 were developed with limited coupling. To achieve this, multiple single DOF MTG models were developed across the range of the secondary DOF. For τ_1, the torque-angle scaling, torque-velocity scaling, and passive function can be determined with respect to θ_1 and $\dot{\theta}_1$. If these functions are determined with respect to θ_1 at specific points of θ_2, then the elevation torque given limited coupling between the two angles is achieved. This is seen in Equation 3.1, where five single DOF MTGs are determined when θ_2 is at 60, 85, 110, 135, and 160 degrees. These angles were chosen in order to span the ROM examined. Linear interpolation between the curve fits was used to determine the torque scaling at points that lay between the discrete values of θ_2.

$$\tau_1 = \tau_{act} \cdot \tau_\omega(\dot{\theta_1}) \cdot \tau_\theta(\theta_1) + \tau_p(\theta_1) \text{ for } \theta_2 = \text{ 60, 85, 110, 135, 160 deg} \tag{3.1}$$

A similar approach was used for the limited coupling case for τ_2. The torque-angle scaling, torque-velocity scaling, and passive scaling for the horizontal plane of elevation torques can be determined with respect to θ_2. The single DOF MTG can be determined at five θ_1 angles (when θ_1 is equal to 0, 30, 60, 90, and 120 degrees) to determine our limited coupling equation for τ_2 (Equation 3.2). Again, the angles of θ_1 were chosen such that the ROM studied was fully examined. Linear interpolation between values of θ_1 was again applied.

$$\tau_2 = \tau_{act} \cdot \tau_\omega(\dot{\theta_2}) \cdot \tau_\theta(\theta_2) + \tau_p(\theta_2) \text{ for } \theta_1 = \text{ 0, 30, 60, 90, 120 deg} \tag{3.2}$$

Next, the position coupling cases were developed for the two torques. In this case, the torque-angle scaling function and passive function are dependent on two angles, while the torque-velocity scaling function is dependent on only one angular velocity. Equations 3.3 and 3.4 below describe the position coupling MTGs for τ_1 and τ_2, respectively.

$$\tau_1 = \tau_{act} \cdot \tau_\omega(\dot{\theta_1}) \cdot \tau_\theta(\theta_1, \theta_2) + \tau_p(\theta_1, \theta_2) \tag{3.3}$$

$$\tau_2 = \tau_{act} \cdot \tau_\omega(\dot{\theta_2}) \cdot \tau_\theta(\theta_1, \theta_2) + \tau_p(\theta_1, \theta_2) \tag{3.4}$$

Finally, an additional step was taken from the position coupling equations to develop models that include both position and velocity coupling. For this case, the torque-angle scaling and passive functions maintain the dependency on two angles as done in the position coupling case, and an additional degree of coupling is added to the torque-velocity scaling function such that it is dependent on two angular velocities instead of one. Equations 3.5 and 3.6 below describe the position and velocity coupling MTGs for τ_1 and τ_2 respectively.

$$\tau_1 = \tau_{act} \cdot \tau_\omega(\dot{\theta_1}, \dot{\theta_2}) \cdot \tau_\theta(\theta_1, \theta_2) + \tau_p(\theta_1, \theta_2) \tag{3.5}$$

$$\tau_2 = \tau_{act} \cdot \tau_\omega(\dot{\theta_1}, \dot{\theta_2}) \cdot \tau_\theta(\theta_1, \theta_2) + \tau_p(\theta_1, \theta_2) \tag{3.6}$$

Table 3.1 offers a summary of the 2 DOF MTG equations developed to explore different degrees of coupling. To explore model accuracy, subject-specific and general models were developed.

Table 3.1: Summary of Coupling Equations

Method	Coupling	Equations
1	limited	$\tau_1 = \tau_{act} \cdot \tau_\omega(\dot{\theta_1}) \cdot \tau_\theta(\theta_1) + \tau_p(\theta_1)$ for $\theta_2 =$ 60, 85, 110, 135, 160 deg $\tau_2 = \tau_{act} \cdot \tau_\omega(\dot{\theta_2}) \cdot \tau_\theta(\theta_2) + \tau_p(\theta_2)$ for $\theta_1 =$ 0, 30, 60, 90, 120 deg
2	θ	$\tau_1 = \tau_{act} \cdot \tau_\omega(\dot{\theta_1}) \cdot \tau_\theta(\theta_1, \theta_2) + \tau_p(\theta_1, \theta_2)$ $\tau_2 = \tau_{act} \cdot \tau_\omega(\dot{\theta_2}) \cdot \tau_\theta(\theta_1, \theta_2) + \tau_p(\theta_1, \theta_2)$
3	$\theta, \dot{\theta}$	$\tau_1 = \tau_{act} \cdot \tau_\omega(\dot{\theta_1}, \dot{\theta_2}) \cdot \tau_\theta(\theta_1, \theta_2) + \tau_p(\theta_1, \theta_2)$ $\tau_2 = \tau_{act} \cdot \tau_\omega(\dot{\theta_1}, \dot{\theta_2}) \cdot \tau_\theta(\theta_1, \theta_2) + \tau_p(\theta_1, \theta_2)$

3.3 Muscle Torque Generator Function Equations

For the different degrees of coupling, different torque-angle scaling, torque-velocity scaling, and passive functions must be developed. As discussed in Chapter 2, a polynomial torque-angle scaling function is a simple and effective function to use for parameter fitting [6, 23]. Therefore, a polynomial curve was used for the limited degree of coupling case for the torque-angle scaling function. For the coupling cases that include position coupling, a polynomial surface was used.

It was found that piecewise functions offer a good representation of the concentric and eccentric torques seen in the torque-velocity scaling function [23]. To maintain a simple model, polynomial curves and surfaces were considered. Therefore, two polynomial curves, one curve for concentric motions when the angular velocity is greater than 0 deg/s and the other for eccentric motions when the angular velocity is less than 0 deg/s, were used for methods that didn't include velocity coupling. For the velocity coupling case, piecewise polynomial surfaces were used. A drawback of the piecewise curves is that while these functions fit well to the data and are continuous, they are not differentiable when $\dot{\theta}$ is zero and are therefore of class C^0.

Since the MTG ROM evaluated is within the ROM of the shoulder, it was expected that passive torques would have a minimal impact [72]. As the double-exponential function is mainly applicable to torques outside the ROM, polynomial curves and surfaces were applied for the passive torque function similarly to what was done for the torque-angle scaling function.

One thing to be noted is that the MTG functions for τ_1 and τ_2 will be different and depend on the data gathered for plane of elevation torques and elevation torques, respectively. As different curves and surfaces can provide a better fit depending on the data, curves and surfaces up to the third-degree were evaluated for the best fit. To avoid overfitting, higher-order curves and surfaces were not considered. For notation, curves will be denoted as m-Curve, where m is the order of the polynomial curve up to 3 and surfaces will be denoted as m, n-Surface where m is the degree of the first independent variable up to 3 and n is the degree of the second up to 3. Equation 3.7 shows an example of a 2,3-Surface torque-angle scaling function and Equation 3.8 shows an example of a torque-velocity scaling function that uses a 2-Curve for the concentric motion and a 1-Curve for the eccentric. The parameters, p are to be fit using experimental data.

$$\tau_\theta(\theta_1, \theta_2) = p_{00} + p_{10}\theta_1 + p_{01}\theta_2 + p_{20}\theta_1^2 + p_{11}\theta_1\theta_2 + p_{02}\theta_2^2 + p_{21}\theta_1^2\theta_2 + p_{12}\theta_1\theta_2^2 + p_{03}\theta_2^3 \quad (3.7)$$

$$\tau_\omega(\dot{\theta}_1) = \begin{cases} p_1\dot{\theta_1}^2 + p_2\dot{\theta}_1 + p_3 & \dot{\theta}_1 \geq 0 \\ \\ p_1\dot{\theta}_1 + p_2 & \dot{\theta}_1 < 0 \end{cases} \quad (3.8)$$

Finally, the activation function must be considered to determine how much τ_1 and τ_2 are contributing to the total force production, where the total torque production, τ, is the sum of the two torque vectors in the direction of α. An activation term approach, similar to that in previous works was applied [6, 33, 51], where the activation torque, τ_{act}, is the product of an activation term (a_1 and a_2 for the plane of elevation and elevation, respectively) and the isometric torque, τ_{max}, for the specified direction. Equation 3.9 shows the activation function for τ_1 or τ_2.

$$\tau_{act_{1,2}} = \tau_{max_{1,2}} a_{1,2} \quad (3.9)$$

Two different approaches were used to determine the activations a_1 and a_2. First, the activations were assumed to be related to the resultant torque direction, α, where the activations had a sine and cosine relationship as seen in Equations 3.10 and 3.11. This was inspired by vector addition, as the magnitude of the two activations will equate to 1. Figure 3.3 shows how a_1 and a_2 change given α for the first activation approach. This ensures that if the motion was only in the plane of elevation, for example, a_1 would go to 1, while a_2 would go to 0 such that there is no elevation torque contribution.

$$a_1 = \cos\alpha \tag{3.10}$$

$$a_2 = \sin\alpha \tag{3.11}$$

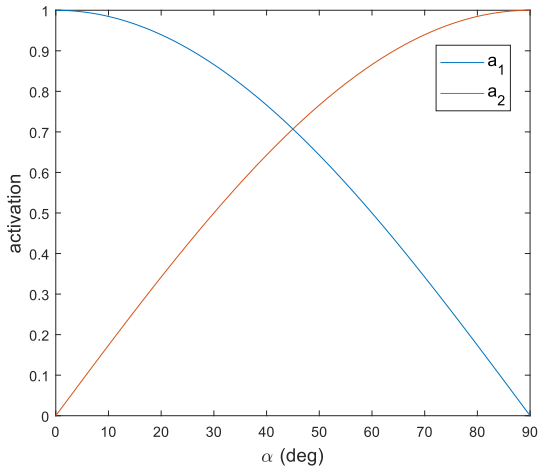

Figure 3.3: The sine and cosine relationship of a_1 and a_2, and the resultant torque direction α for the first activation approach.

The second activation approach solved for independent activations directly from experimental isokinetic data, operating under the assumption that activations a_1 and a_2 are constant in time for a given α. Since the data is isokinetic and does not contain angular dependencies, the standard form of the MTG (Equation 2.1) can be simplified to the form expressed in Equation 3.12. The activation torques for a direction are expressed using Equation 3.9. If the activations are constant, then the component torques τ_1 and τ_2 of the isokinetic torques are equivalent to the isometric torque for the component torque direction, τ_{max}, the activation for the direction for the given α, a_α, and an unknown torque-velocity scaling function that is dependant on the angular velocity in the direction of α, $s(\omega_\alpha)$. Equation 3.13 expresses this relationship for a plane of elevation torque. Further details of this approach are outlined in Chapter 4.

$$\tau(\omega) = \tau_{act} \cdot \tau_\omega(\omega) \tag{3.12}$$

$$\tau_1 = \tau_{max_1} \cdot a_{1_\alpha} \cdot s(\omega_\alpha) \tag{3.13}$$

Chapter 4

Shoulder Experiments

The contents of this chapter describe the methods to collect and process data used to fit subject-specific and general MTG functions for the shoulder. In order to develop the functional coupling MTG equations outlined in Section 3.1, experimental data was gathered to generate equations for the torque-angle scaling, torque-velocity scaling, and passive functions.

4.1 Setup

4.1.1 System Used

Testing was conducted using the Biodex System 4 Pro^{TM} (Biodex Medical Systems, Inc, Shirley, NY). The Biodex is a computerized dynamometer that is used in sports and orthopedic medicine, neurorehabilitation, and research. The Biodex allows for a specific joint in the body to be isolated, and the net joint torque can be measured in different modes of operation. For this study specifically, the shoulder joint was isolated and the isometric, isokinetic, and passive modes were utilized to measure the net shoulder torques.

4.1.2 Joint Alignment

To ensure accurate torque measurements, the axis of the Biodex must be aligned with a participant's anatomical joint center [27]. The Shoulder Joint Center (SJC) can be

approximated as 10.4% of the distance from the acromion to the radiale, with the three-dimensional position lying on the longitudinal axis between the two bony landmarks [13]. Participants' bony landmarks were palpated and the 10.4% distance was marked. The Biodex was fitted with a custom 3D-printed part that secured a laser pointer in the center of the Biodex crank. The laser pointer was used to align the Biodex crank center with the marker at the participant's SJC. Work done in [5] has shown that the SJC is often not stationary throughout the movement. The movement of the SJC can be attributed to the fact that shoulder joint mobility is not only the motion of the glenohumeral joint, but is also the motion of the scapula gliding along the thorax, also known as scapulothoracic-gliding [66]. Until 120 degrees in elevation, shoulder mobility is due to the glenohumeral joint. However, past this, the motion is also a result of scapular gliding. This can contribute to the movement of the SJC at higher elevations. To minimize the movement of the SJC, all participants were instructed to keep their back (with a specific focus on the scapula) against the seat of the Biodex. Two straps, one across each participant's shoulder was used to prevent movement outside of the shoulder joint during testing. Participants were also instructed to keep their elbow and wrist joints locked in a neutral and straight position.

With the alignment process mentioned, the Biodex crank angle measurement was used as the shoulder angle, as done in the previous Biodex testing by Brown [5]. In this work, an electrogoniometer was used to determine if there was any discrepancy between the Biodex crank angle measurement and the angle of the elbow joint. It was determined that the Biodex crank angle was an accurate representation of the elbow joint angle, most likely due to the rigid handle that connected the person and the Biodex. The shoulder joint and elbow joint used the same rigid attachment, and therefore Brown used the Biodex crank angle as a measurement of the shoulder, instructing participants to keep their back against the seat similarly to what was done for this work. The same grip attachment was used in this study, and therefore the Biodex crank angle measurements were also used as the shoulder joint angle.

4.2 Elevation Torque Data

The testing was broken down into three main sections: elevation torque, in which the participant applied torque in the direction of θ_2 for isometric and passive tests, plane of elevation torque, where the participant applied torque in the direction of θ_1 for isometric and passive tests, and isokinetic tests, which vary the degree of elevation and plane of elevation torques by changing the Biodex axis tilt, effectively changing α. This section focuses on the elevation torques gathered.

4.2.1 Subjects

10 males (24 ± 4 years, 1.79 ± 0.08m, 78.2 ± 7.6kg) and 10 females (22 ± 7 years, 1.63 ± 0.06 m, 59.6 ± 8.2 kg) participated in the study. The eligibility criteria of the study ensured that participants had not experienced any pain during activities of daily living within the past 6 months, as well as ensured that the participant did not have any shoulder pain or an existing heart condition. The participants also did not have any prior experience with the Biodex System. Ethics approval was obtained from the University of Waterloo Research Ethics Board (REB 44157).

4.2.2 Isometric Test

For the isometric testing mode, the attachment arm of the Biodex was moved to a specific elevation to achieve a specific θ_2, and the chair of the Biodex was rotated to achieve different planes of elevation, θ_1. The Biodex attachment arm then remained stationary while the participant used their Maximum Voluntary Contraction (MVC) for 5 seconds. Isometric torque was measured in elevation for 25 different combinations of θ_1 and θ_2. θ_1 was measured at 0, 30, 60, 90, and 120 degrees and θ_2 was measured at 60, 85, 110, 135, and 160 degrees. Three minutes of rest were given to participants between every five exertions with more on request to prevent the participant from fatiguing. Figure 4.1 shows an example of the setup of an isometric test in elevation when θ_1 is 0 degrees and θ_2 is 85 degrees.

4.2.3 Passive Test

In the passive testing mode, the chair of the Biodex was rotated to achieve a specific plane of elevation, θ_1, and the Biodex was set to elevate the participant's arm across the ROM studied (60 deg $\leq \theta_2 \leq$ 160 deg). The Biodex moved the participant's arm at a rate of 5 deg/s while the participant provided no torque in order to measure only the passive torques in the shoulder resisting the motion. Five passive tests were done, measuring the ROM of θ_2 for θ_1 at 0, 30, 60, 90, and 120 degrees.

Figure 4.1: Example of a participant setup when θ_1 is 0 deg and θ_2 is 85 deg for isometric testing in elevation

4.3 Plane of Elevation Torque Data

4.3.1 Subjects

7 male (26 ± 3 years, 1.80 ± 0.07m, 79.0 ± 7.7kg) and 6 female (24 ± 6 years, 1.63 ± 0.07m, 59.5 ± 6.3kg) subjects who participated in the elevation torque data collection were able to return and participate in the plane of elevation torque section of the study. The eligibility criteria for the study remained the same.

4.3.2 Isometric Test

For the isometric tests, the chair of the Biodex was lowered such that the participant was lying horizontally. The attachment arm of the Biodex was moved to different positions, which corresponded to a different plane of elevation angle, θ_1. The tilt of the Biodex axis was modified such that different elevation angles, θ_2, could be achieved. Similar to the elevation torque isometric study, the Biodex attachment arm remained stationary at specified angles, and MVC was used for 5 seconds at each of these positions. Isometric torques were measured in the plane of elevation for 25 different combinations of θ_1 and θ_2. θ_1 was measured at 0, 30, 60, 90, and 120 degrees and θ_1 was measured at 70, 85, 110, 135,

and 160 degrees. 70 degrees elevation was measured for the plane of elevation isometric torques instead of the 60 degrees in the elevation isometric torques as the Biodex axis was unable to tilt past 70 degrees. Extrapolation using the resulting MTG functions can be done to determine torques produced at 60 degrees of elevation if required. Figure 4.2 shows an example of the setup of a plane of elevation isometric test when θ_1 is 0 deg and θ_2 is 85 deg.

Figure 4.2: Example of a participant setup when θ_1 is 0 deg and θ_2 is 85 deg for the plane of elevation isometric testing.

4.3.3 Passive Test

In the passive testing mode, the lowered chair position was maintained, and the axis of the Biodex was tilted to achieve specific elevations, θ_2. The Biodex was set to move the participant's arm across the plane of elevation for the ROM studied (0 deg $\leq \theta_1 \leq$ 120 deg). Similar to the previous passive study, the participant was instructed not to provide any torque so that only passive torques were measured, and the Biodex moved the participant's arm at 5 deg/s. Five passive tests were done measuring the ROM of θ_1 for θ_2 at 70, 85, 110, 135, and 160 degrees.

4.4 Isokinetic Data

The same 20 individuals who participated in the elevation torque data collection also participated in gathering the isokinetic data. For the isokinetic testing, the Biodex was set up so that the participant was first in forward flexion (with the Biodex axis having a tilt of 0 degrees and θ_1 having a constant angle of 90 degrees). The participant was then instructed to apply their MVC in a concentric motion followed by an eccentric motion while the Biodex limited the speed they were able to achieve. Speeds of 5, 10, 20, 30, and 45 deg/s were used to cover speeds applicable for slow to medium lifting and reaching motions (as previous studies found maximum speeds to range from 80 to 200 deg/s [41]). While in forward flexion, $\dot{\theta_2}$ was individually measured as the participant strictly elevated their arm. The axis of the Biodex was then tilted 30 and 60 degrees from the vertical (with the participant's arm moving diagonally away from their chest in concentric motions) to measure the combination of $\dot{\theta_1}$ and $\dot{\theta_2}$. Finally, the Biodex axis was tilted to 90 degrees such that only $\dot{\theta_1}$ was measured in a horizontal plane of elevation motion. The same speeds mentioned above were applied to all angles. In total, 20 concentric and 20 eccentric combinations of $\dot{\theta_1}$ and $\dot{\theta_2}$ were measured. Figure 4.3 shows an example of a participant setup when the Biodex axis is tilted 30 degrees from the vertical.

Figure 4.3: Example of a participant setup when the Biodex axis is tilted 30 deg from the vertical. The participant was limited to 5 deg/s, resulting in a $\dot{\theta_1}$ of 2.5 deg/s and a $\dot{\theta_2}$ of 4.3 deg/s for the trial.

The participant was limited to 5 deg/s for the specific test shown in 4.3, resulting in a $\dot{\theta_1}$ of 2.5 deg/s and a $\dot{\theta_2}$ of 4.3 deg/s. Participants were given three minutes of rest

between every 5 concentric and eccentric pairs, with more rest given upon request. With low velocity tests, participants found it very tiring to reach high eccentric torques, and were given additional rest after these trials. This was similarly found by Yeadon *et al.* [73], again leading to the theory that maximal contraction is avoided during eccentric motions as a means of injury prevention. Therefore, while participants were encouraged to produce their MVC, it is possible that this was not achieved during eccentric motions.

4.5 Data Processing

First, a 6 Hz low-pass 2nd-order Butterworth filter was applied to all torque data gathered to remove noise [8]. Next, different processing techniques were applied to the different data types. The following paragraphs outline the data processing techniques that were used on the different types of biomechanical torque data.

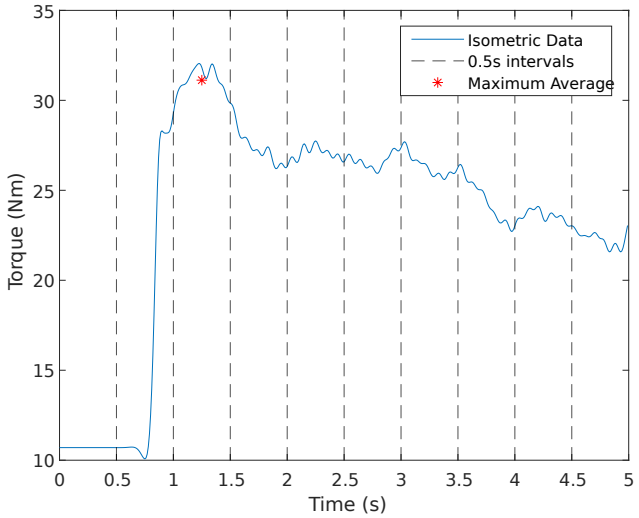

Figure 4.4: Example of a participant's isometric toque results for a 5s contraction. The highest average torque is found over 0.5s intervals to determine the isometric torque for the specific angle.

The plane of elevation and elevation isometric torques at a specific angle for each participant were determined by selecting the highest average torque over 0.5 second intervals, as done in [55]. An example of the method used to find the isometric torque at a specific

angle can be seen in Figure 4.4. The isometric torques were then normalized by each individual's maximum isometric torque in either plane of elevation or elevation to allow for a fair comparison between individuals of different strengths.

For the isokinetic torque results, a function was first applied that removed torque data that was less than 70% of the target angular velocity, as done in [5]. The maximum and average joint torques were then found for each concentric and eccentric angular velocity trial. The final isokinetic torques for a participant were then found by regressing the maximum torque values against the average torque values to create a maximal dataset as described in [73]. The maximal dataset provides sets of torque and angular velocity values with less noise and ensures that the torque values no longer have angular dependencies. An example of the regression used to replace the isokinetic torque value can be seen in Figure 4.5.

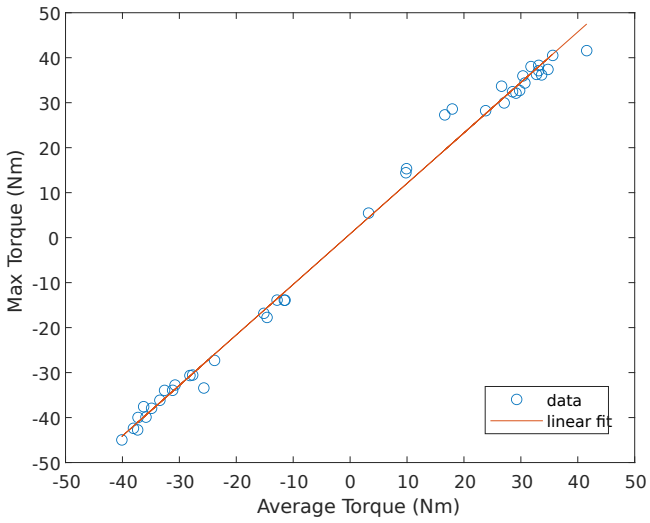

Figure 4.5: Example of regression used to create a maximal isokinetic dataset.

The components of the angular velocity along the $\dot{\theta}_1$ and $\dot{\theta}_2$ axes were found using the Biodex axis tilt angle and simple trigonometry. For isokinetic torques not measured strictly along the plane of elevation or elevation axis, the components of the total torque, τ_1 and τ_2 were also determined using the Biodex axis tilt angle and trigonometry. For Method 1 and Method 2 that used no velocity coupling, the isokinetic torques were normalized by the maximum isometric torque in the same direction. For Method 3 with velocity coupling, the components of the maximum total torque cannot simply be divided by the maximum isometric torque in the same direction as the muscle activation may not be

maximum for the given α, resulting in an unfair comparison between torques gathered in pure plane of elevation or pure elevation. Rearranging Equation 3.12 which gives torque for an isokinetic test, the measured torque can be divided by the activation torque, τ_{act}, to give the torque-velocity scaling function. This essentially divides the component isokinetic torques by the activation and the maximum isometric torque for the direction, allowing for a fair comparison to be made.

The normalized maximum isometric and isokinetic torques (normalized by τ_{max}) were then plotted in a box plot for each participant to visualize outliers in a participant's normalized torque values. Outliers are defined as being more than 1.5 times the Interquartile Range (IQR) above or below the upper and lower quartile. Figure 4.6 shows the result of the box plot for the 20 participants used in the isometric elevation and isokinetic tests. The outliers, which are shown as red crosses, were removed from the data set.

The passive torques were then analysed. The Biodex removes the contribution of gravity torque using the weight of a participant's limb for isometric and isokinetic tests; however, this feature is not available for passive torques. Therefore, additional processing is required to remove the contribution of gravitational torques. A trial using the Biodex attachment arm only was first run, as this results in the gravitational and inertial torques from the attachment. The mass, moment of inertia, and center of gravity of the Biodex attachment can then be solved for using least-squares fitting. This information, along with the previously measured participant limb weight from the isometric studies, can be combined to remove the contribution of the gravity torques, resulting in the passive torques. In cases where the Biodex axis is tilted, the gravity torques are projected onto the plane of rotation as the Biodex only measures torques in this plane. Once the passive torques were obtained, no normalization is required as the passive torques are not dependent on an individual's strength and instead on the passive structures such as ligaments in the shoulder.

As previously mentioned in Chapter 3, two different activation assumptions were examined. The first assumes that the activations a_1 and a_2 are related using cosine and sine functions as outlined in Equations 3.10 and 3.11. The second approach solved for the independent activations directly using the isokinetic data. To solve for these activations, 5 male and 5 female participants were used, leaving the remaining dataset to solve for the coupled torque-velocity scaling function required for Method 3.

As shown in Equation 3.13, a component of the total isokinetic torque (the component being in the direction of τ_1 or τ_2) measured at a given α can be expressed as the isometric torque for the given direction, an unknown torque-velocity scaling function, and the activation for the direction that is assumed to be constant for α. Four different ratios between two data points were created for the five isokinetic torques measured for a given α. As

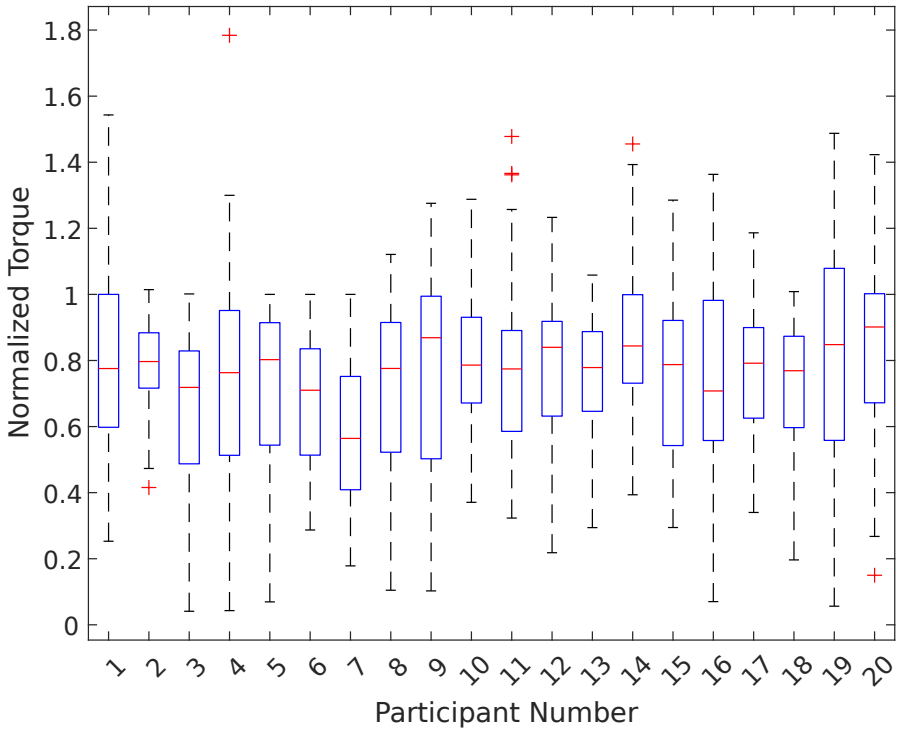

Figure 4.6: Box plot of each participant's normalized torque data (normalized by τ_{max}) used to identify outliers. The median is represented by the red bar, the upper and lower quartiles by the box, the maximum and minimum values excluding outliers by the dotted lines, and the outliers by the red crosses.

the isometric torque and the activation are constant, they canceled out and the result is a ratio of the isokinetic torques measured at two points which is equivalent to a ratio of the polynomial scaling curve that is evaluated at the two points. Equation 4.1 shows an example of the ratio used for plane of elevation torques for data point i and j.

$$\frac{\tau_{1_i}}{\tau_{1_j}} = \frac{s_i(\omega_\alpha)}{s_j(\omega_\alpha)} \tag{4.1}$$

Using curve fitting, it was determined that a cubic relationship resulted in the best fit for the scaling function $s(\omega_\alpha)$. Optimization was then used to solve for the four coefficients of the unknown scaling function, minimizing the difference between the torque ratios and the ratios of the scaling functions. Once the coefficients of the scaling function were determined for a given α, a second round of optimization was conducted to solve for the activation, using Equation 3.13 to minimize the difference between the experimental component torques and the calculated torques. This was done for a completely general dataset, a female dataset and a male dataset. The process was also repeated for concentric and eccentric data, to follow the theory that less activation is used in eccentric motion [73]. The concentric results of the activations given α can be seen in Figure 4.7 and the eccentric results are seen in Figure 4.8. As expected, the activation results are lower for eccentric motion compared to concentric. One interesting point to note is that the results of the completely general concentric activations in Figure 4.7 are not unlike like activation assumptions used in the first activation approach (see Figure 3.3). In the future, more data points should be considered for a more robust solution.

At this point, the isometric, isokinetic and passive data could either be used as is for subject-specific models, or the mean from the population at each angle and angular velocity combination could be determined for completely general, female general and male general models. Chapter 5 details how the processed torque data was used to fit the MTG functions for the different coupling equations.

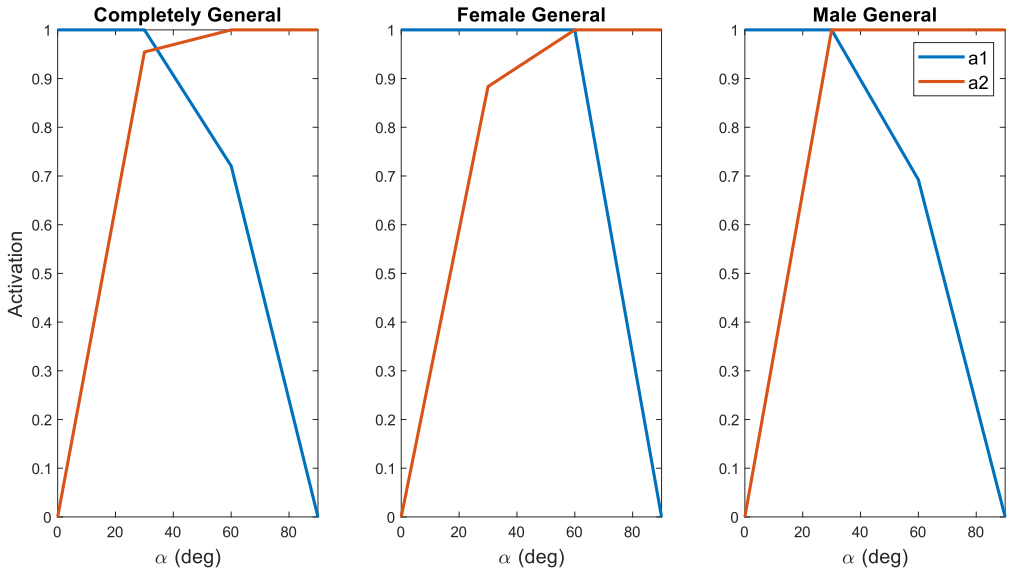

Figure 4.7: Concentric activations for a given α for the completely general model, the female general model and the male general model.

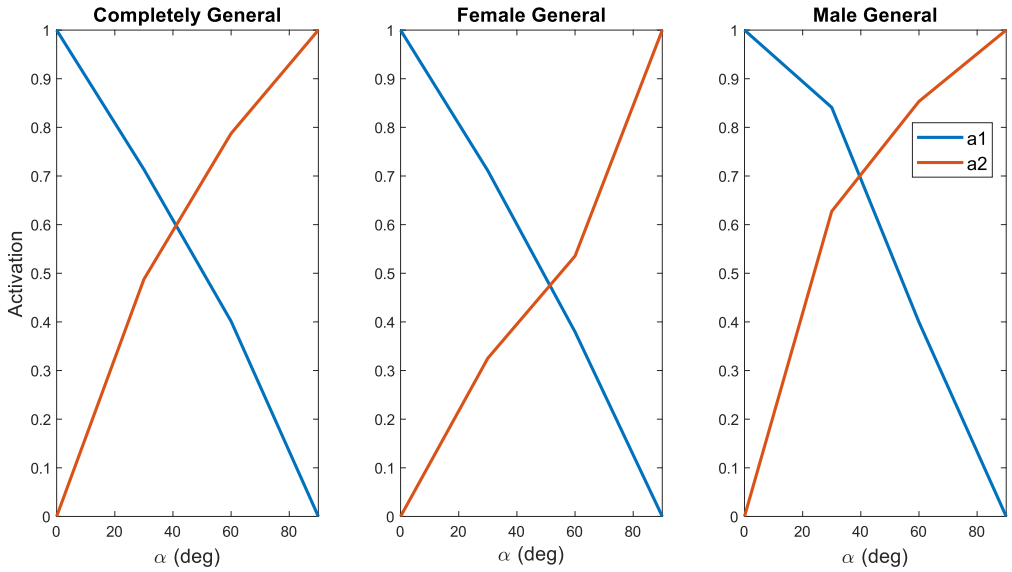

Figure 4.8: Eccentric activations for a given α for the completely general model, the female general model and the male general model.

Chapter 5

Multi-Degree-of-Freedom Muscle Torque Generator Model Fitting and Comparison

The maximum elevation and plane of elevation isometric torques, the maximum isokinetic torques, and the passive torque were used to fit the MTG functions from Chapter 3 for the different coupling cases. First, the methods of fitting parameters for the different MTG functions using the experimental data are outlined. Next, the results of the curve and surface fits are presented and discussed for τ_1 and τ_2. The complete model results are then compared against experimental data for the general and subject-specific cases. Finally, the results of the models are compared and discussed.

5.1 Parameter Fitting

Using the processed experimental data, the different curves and surfaces outlined in Chapter 3 were applied to determine the best type of fit for the data, as well as the resulting parameters for the fit. First, the method of the curve and surface fits are described, followed by the fitting results.

5.1.1 Methods

In total, 36 best curves and surface fits were found to evaluate the different degrees of coupling for the three methods. Five best curve fits were found for the torque-angle scaling function as well as the passive torque function in the limited coupling case for τ_1 when θ_2 was 85, 110, 135, and 160 degrees. The same was done for τ_2, and the best curve fits were determined when θ_1 was equal to 0, 30, 60, 90, and 120 degrees. Two curves, one for concentric motion and eccentric motion were found for both τ_1 and τ_2 in methods that did not include velocity coupling (Methods 1 and 2). A surface that was in terms of θ_1 and θ_2 was found for the torque-angle scaling function and the passive function for both τ_1 and τ_2 in methods that included position coupling (Methods 2 and 3). Finally, for the velocity coupling case, two surfaces, one for concentric motion and the other for eccentric, were found for the torque-velocity scaling functions for both τ_1 and τ_2. As activations are considered in the data processing for Method 3, the number of surface fits was doubled for the coupled torque-velocity scaling functions so that both activation methods were considered. The functions and number of best curves/surfaces found for those functions are summarized in Table 5.1, where the subscript after the MTG function type indicates whether the function is for τ_1 or τ_2.

MATLAB's Curve Fitting Toolbox^{TM} was used to find the curve or surface that best fits the experimental data for a given function. Polynomial curves and surfaces in the toolbox fall under the regression model group, where the default fit method is a linear least squares method. To avoid overfitting the data, curve and surface fits were only evaluated to the third degree; therefore three different curves were evaluated for the functions without coupling, and nine different surfaces were evaluated for the functions with coupling. The torque-angle and passive functions were fit using the default methods. For the torque-velocity scaling functions, an additional constraint was added to ensure that the curves and surfaces had an intercept at one when the angular velocity was equal to zero. In previous piecewise torque-velocity scaling models [3, 23, 73], there is a constraint at this point as isometric torques are achieved when the angular velocity is zero, and therefore no torque-velocity scaling is required. To ensure that this criterion was met, and to ensure that there was no C^0 discontinuity between the piecewise models, the intercept constraint was set. An example of the constraint can be seen in Figure 5.1, where the concentric and eccentric curves meet at the intercept of 1.

For subject-specific models, the Root Mean Square Percentage Error (RMSPE) was calculated for each curve and surface fit. The fit with the least amount of error was then selected as the fit for that model. 13 subject-specific models were evaluated, as only 13 participants completed the study for both the elevation and plane of elevation isometric

Table 5.1: Summary of Muscle Torque Generator Functions and the Number of Best Curves and Surfaces Fit

Function	Number of Curves/Surfaces
$\tau_{\theta_1}(\theta_1)$	5 Curves
$\tau_{\theta_2}(\theta_2)$	5 Curves
$\tau_{p_1}(\theta_1)$	5 Curves
$\tau_{p_2}(\theta_2)$	5 Curves
$\tau_{\omega_1}(\dot{\theta_1})$ Con.	1 Curve
$\tau_{\omega_1}(\dot{\theta_1})$ Ecc.	1 Curve
$\tau_{\omega_2}(\dot{\theta_2})$ Con.	1 Curve
$\tau_{\omega_2}(\dot{\theta_2})$ Ecc.	1 Curve
$\tau_{\theta_1}(\theta_1, \theta_2)$	1 Surface
$\tau_{\theta_2}(\theta_1, \theta_2)$	1 Surface
$\tau_{p_1}(\theta_1, \theta_2)$	1 Surface
$\tau_{p_2}(\theta_1, \theta_2)$	1 Surface
$\tau_{\omega_1}(\dot{\theta_1}, \dot{\theta_2})$ Con.	2 Surfaces
$\tau_{\omega_1}(\dot{\theta_1}, \dot{\theta_2})$ Ecc.	2 Surfaces
$\tau_{\omega_2}\dot{\theta_1}, \dot{\theta_2})$ Con.	2 Surfaces
$\tau_{\omega_2}(\dot{\theta_1}, \dot{\theta_2})$ Ecc.	2 Surfaces

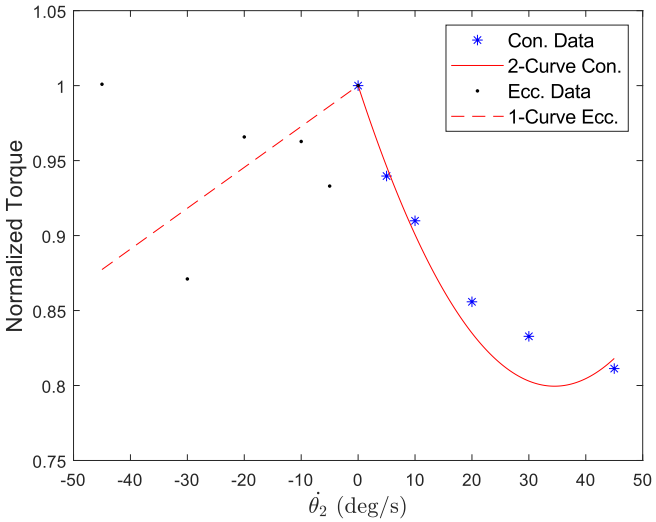

Figure 5.1: Example of a piecewise torque-velocity scaling function curve fit with an intercept constraint at 1 when $\dot{\theta}_2 = 0$. The solid line in red represents a second-degree curve fit to the concentric data. The dashed red line represents the linear fit for the eccentric data.

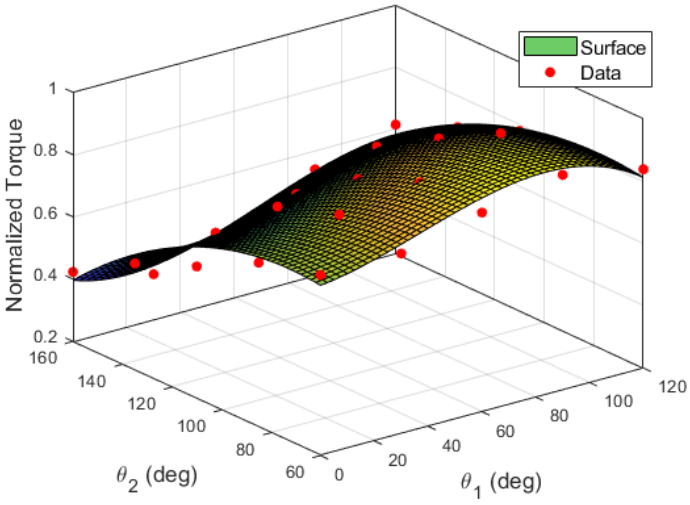

Figure 5.2: Example of a surface fit used for the torque-angle scaling function. A 3,2-Surface was found to be the best fit for the experimental data.

and passive torques. General models were also created, a completely general model based on all participant data, a general model based on female participant data, and a general model based on male participant data. To determine the curves and surfaces that best fit the general models, k-fold cross validation was used. K-fold cross validation is a method where the data is partitioned into folds, and (k-1) folds are used to create the model while the remaining fold is used to validate the model [35]. Typically, k-values of 5 and 10 are used, and the process described above is iterated a total of k-times. For the general models, a k-value of 10 was used, and the average RMSPE of the 10-folds was determined for a specific curve or surface fit. The best fit was the curve or surface with the lowest error. An example of a surface fit for the torque-angle scaling function can be seen in Figure 5.2. The best fit surface to the data presented was determined to be a 3,2-Surface. It should be noted that separate RMSPEs are calculated for concentric and eccentric motions as different curves are applied.

5.1.2 Fitting Results

The methods described above were applied to the three general models evaluated, and the 13 subject-specific models. The results of the curve and surface fits along with the accuracy of the fits are presented below.

General Model Results

The curve and surface fit results for the three general models are displayed in Table 5.2. As k-fold cross validation was used to determine the curves and surfaces that best fit the models, the RMSPE is the average error of the folds. As five different curves were used for the first four functions in the table ($\tau_{\theta_1}(\theta_1)$, $\tau_{\theta_2}(\theta_2)$, $\tau_{p_1}(\theta_1)$, $\tau_{p_2}(\theta_2)$), the average RMSPE of the curves was presented. The median curve type was also presented for the first four functions. A1 and A2 for the final eight functions in the table indicate whether the first or second activation method was applied. As the torque-angle and torque-velocity scaling functions give normalized torque, percentage error was chosen to display the difference between the unitless values. A higher percentage error indicates that the curve or surface fit results in a scaled normalized torque that is farther from the experimental data. The passive torque function does not produce a normalized value and to compare the accuracy with the other MTG functions, the passive torques were normalized by the absolute maximum passive torque for either the plane of elevation or elevation torques of a model. This allowed for the calculation of the RMSPE of the passive torques. The absolute maximum passive torques for τ_1 for the completely general, female general and male general model

were 8.2 Nm, 8.3 Nm and 8.5 Nm, respectively. For τ_2, the absolute maximum torques for the completely general, female general and male general model were 4.3 Nm, 4.9 Nm and 4.9 Nm, respectively.

Looking at the curve and surface fits for the torque-angle scaling function, it is seen the most common fit for θ_1 in the limited coupling case ($\tau_{\theta_1}(\theta_1)$) across the three general models is a 3-Curve, showing that a cubic function best describes the torque-angle relationship in the plane of elevation. The most common fit for θ_2 in the limited coupling case ($\tau_{\theta_2}(\theta_2)$) across the three general models is a 2-Curve, showing that a quadratic relationship best describes the impact of θ_2 in elevation. The fits of these curves also result in the lowest RMSPE for each model compared to all other function types. This indicates that participants showed more reproducible results using an isometric elevation motion compared to isometric plane of elevation or isokinetic motions. The cubic and quadratic relationship is also reflected in the torque-angle scaling for the position coupling case for both plane of elevation torques, and elevation torques ($\tau_{\theta_1}(\theta_1, \theta_2)$, $\tau_{\theta_2}(\theta_1, \theta_2)$) in the completely general model, the general female model, and the male general model, where the impact that θ_1 and θ_2 are best described using 3 and 2 degrees for the surface, respectively. The exception to this finding is in the female general model for elevation torques ($\tau_{\theta_2}(\theta_1, \theta_2)$), where θ_1 is better represented using 1 degree. A comparison between the completely general model and the female general model for the position-coupled torque-angle scaling function in elevation ($\tau_{\theta_2}(\theta_1, \theta_2)$) can be seen in Figure 5.3. It has previously been shown that there are differences in how women and men activate their shoulder muscles under isometric loading, with women typically showing a lower muscle activation in muscles that act in the primary force direction and more activation in other muscles [2]. The differences in muscle activation in isometric loading could explain why the female general model is presenting different curve fitting results from the completely general and male general models.

Evaluating the curve and surface fits for the torque-velocity scaling function, it can be seen that there is more variability between the fit types. On average, a higher RMSPE is found for curves and surfaces fit to eccentric data compared to concentric data, although this is not always the case. As previously mentioned, participants found it difficult to reach high torques in eccentric motion, and most likely did not use their MVC as discussed in [73]. This led to wide-spread eccentric torque data with less of a trend, and only increased above the concentric torque in the male general model, resulting in a torque that was lower compared to what previous models predicted [3, 23, 46].

For the torque-velocity scaling function without coupling in the plane of elevation ($\tau_{\omega_1}(\dot{\theta}_1)$), a cubic relationship was determined for both the concentric and eccentric motions. An example of the cubic relationship is displayed in Figure 5.4, where the torque-velocity scaling function in the plane of elevation is plotted for the female general model.

Table 5.2: General Muscle Torque Generator Functions Fitting Results and Accuracy

	All		Female		Male	
Function	Fit Type	RMSPE	Fit Type	RMSPE	Fit Type	RMSPE
$\tau_{\theta_1}(\theta_1)$	3-Curve	14.0%	3-Curve	15.2%	3-Curve	14.4%
$\tau_{\theta_2}(\theta_2)$	2-Curve	9.3%	2-Curve	12.5%	3-Curve	13.2%
$\tau_{p_1}(\theta_1)$	3-Curve	36.4%	3-Curve	38.3%	3-Curve	32.0%
$\tau_{p_2}(\theta_2)$	3-Curve	47.9%	3-Curve	48.6%	3-Curve	61.8%
$\tau_{\omega_1}(\dot{\theta_1})$ Con.	3-Curve	23.3%	3-Curve	25.9%	3-Curve	21.5%
$\tau_{\omega_1}(\dot{\theta_1})$ Ecc.	3-Curve	20.9%	3-Curve	20.6%	3-Curve	22.3%
$\tau_{\omega_2}(\dot{\theta_2})$ Con.	2-Curve	10.5%	1-Curve	14.6%	2-Curve	14.1%
$\tau_{\omega_2}(\dot{\theta_2})$ Ecc.	1-Curve	17.5%	2-Curve	25.2%	1-Curve	21.8%
$\tau_{\theta_1}(\theta_1, \theta_2)$	3,2-Surface	14.7%	3,2-Surface	15.6%	3,2-Surface	15.0%
$\tau_{\theta_2}(\theta_1, \theta_2)$	3,2-Surface	10.3%	1,2-Surface	13.3%	3,2-Surface	14.5%
$\tau_{p_1}(\theta_1, \theta_2)$	3,2-Surface	38.7%	3,1-Surface	39.4%	1,1-Surface	38.1%
$\tau_{p_2}(\theta_1, \theta_2)$	2,3-Surface	50.6%	1,3-Surface	49.0%	2,3-Surface	63.7%
$\tau_{\omega_1}(\dot{\theta_1}, \dot{\theta_2})$ Con. A1	1,2-Surface	28.9%	1,1-Surface	29.6%	2,3-Surface	25.8%
$\tau_{\omega_1}(\dot{\theta_1}, \dot{\theta_2})$ Ecc. A1	2,1-Surface	26.0%	1,1-Surface	32.9%	1,1-Surface	22.3%
$\tau_{\omega_2}(\dot{\theta_1}, \dot{\theta_2})$ Con. A1	3,2-Surface	19.7%	3,1-Surface	24.4%	1,3-Surface	15.9%
$\tau_{\omega_2}(\dot{\theta_1}, \dot{\theta_2})$ Ecc. A1	3,1-Surface	26.1%	2,1-Surface	29.5%	1,1-Surface	23.1%
$\tau_{\omega_1}(\dot{\theta_1}, \dot{\theta_2})$ Con. A2	1,3-Surface	20.5%	3,2-Surface	13.0%	1,3-Surface	23.1%
$\tau_{\omega_1}(\dot{\theta_1}, \dot{\theta_2})$ Ecc. A2	1,1-Surface	28.3%	3,1-Surface	37.2%	2,2-Surface	19.4%
$\tau_{\omega_2}(\dot{\theta_1}, \dot{\theta_2})$ Con. A2	3,1-Surface	15.0%	3,1-Surface	16.4%	3,1-Surface	14.6%
$\tau_{\omega_2}(\dot{\theta_1}, \dot{\theta_2})$ Ecc. A2	3,1-Surface	23.1%	2,3-Surface	54.6%	3,1-Surface	20.7%

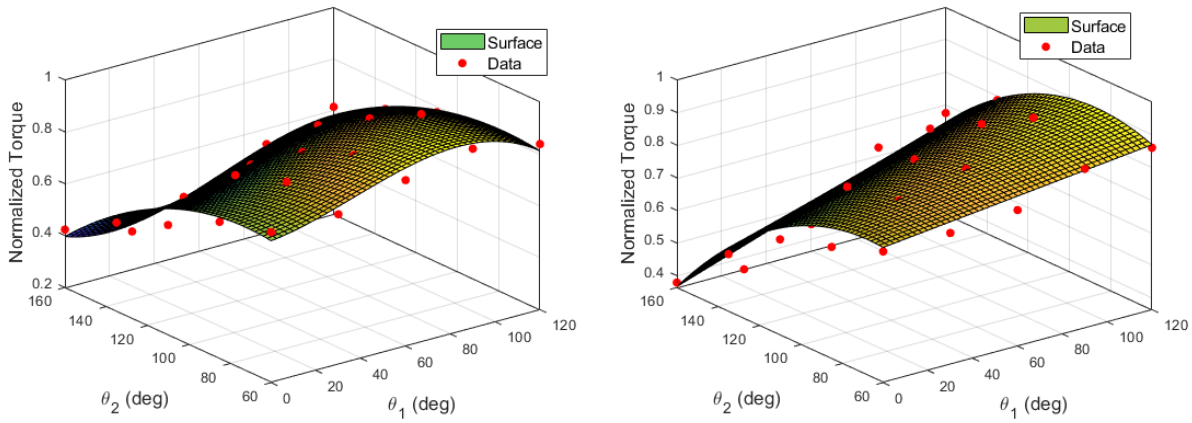

(a) 3,2-Surface General Model

(b) 1,2-Surface Female General Model

Figure 5.3: Comparison of the completely general and female general model for the position-coupled torque-angle scaling function in elevation ($\tau_{\theta_2}(\theta_1, \theta_2)$).

Due to a lack of repeated trials (repeated trials were not conducted to reduce participant fatigue), it is likely that the cubic curves are overfitting the data. K-fold cross validation was used to determine the RMSPE for the curves and to help mitigate overfitting. In Figure 5.4, a lower error was determined for eccentric motion compared to concentric using k-fold cross validation. When the curves are compared against the mean experimental data of the group, the eccentric appears to have a higher error. However, the k-fold cross validation indicates that the 3-Curve was a more general model for the data subsets compared to if the data was fit only to the experimental mean. Percent errors ranging from 20.6-25.9% are observed for the concentric and eccentric curves. This indicates that the Root Mean Square Error (RMSE) between the normalized experimental torques and the torques scaled by the torque-velocity scaling function range between 0.206-0.259. Participants expressed more fatigue when completing isokinetic tasks compared to isometric tasks, which could have led to inconsistencies between participants and result in the higher error achieved compared to the torque-angle scaling functions.

For the torque-velocity scaling function without coupling in the place of elevation ($\tau_{\omega_2}(\dot{\theta}_2)$), a quadratic relationship was the most common for concentric elevations, and a linear relationship was the most common for eccentric elevations. A different curve fit was seen in the female general model, with a linear fit applied to concentric motions and a quadratic for eccentric in elevation. A comparison of the female general model and male general model for the torque-velocity scaling function in elevation is shown in Figure

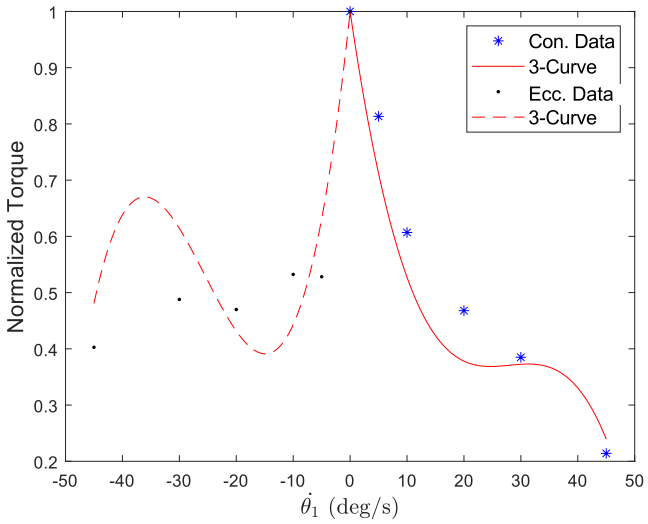

Figure 5.4: Example of a 3-Curve fit for the torque-velocity scaling function in the plane of elevation ($\tau_{\omega_1}(\dot{\theta}_1)$) for the female general model.

5.5. The comparison shows that the male population was able to produce higher eccentric torques on average compared to the female population, resulting in the difference in fits.

For the torque-velocity scaling functions with coupling, the two different activation methods (A1 and A2) were considered as seen in Table 5.2. For the first activation method in the plane of elevation ($\tau_{\omega_1}(\dot{\theta}_1, \dot{\theta}_2)$), less of a trend is displayed between the three general models. Surfaces with 1 degree for $\dot{\theta}_1$ are the most common for concentric and eccentric motions, and for $\dot{\theta}_2$ 1 degree is most common for eccentric motion. For the first activation method in elevation ($\tau_{\omega_2}(\dot{\theta}_1, \dot{\theta}_2)$), surfaces with 3 degrees for $\dot{\theta}_1$ are most common for concentric motion, and for $\dot{\theta}_2$ 1 degree surfaces are the most common in eccentric motion. For the second activation method in plane of elevation ($\tau_{\omega_1}(\dot{\theta}_1, \dot{\theta}_2)$), there are also limited trends between the models. Surfaces with 1 degree for $\dot{\theta}_1$ are the most common for concentric motions, and for $\dot{\theta}_2$ 1 degree is most common for eccentric motion. For the second activation method in elevation ($\tau_{\omega_2}(\dot{\theta}_1, \dot{\theta}_2)$), a 3,1-Surface was seen across all concentric and eccentric fits, with the exception being a 2,3-Surface for the eccentric female model. The higher errors seen in the female general model for the second activation method could be due to the addition of activations which rely on assumptions. It is possible that the activations calculated for the female general model do not accurately represent the muscle activations of the population.

Overall, a wider spread of data is seen for the isokinetic measurements compared to

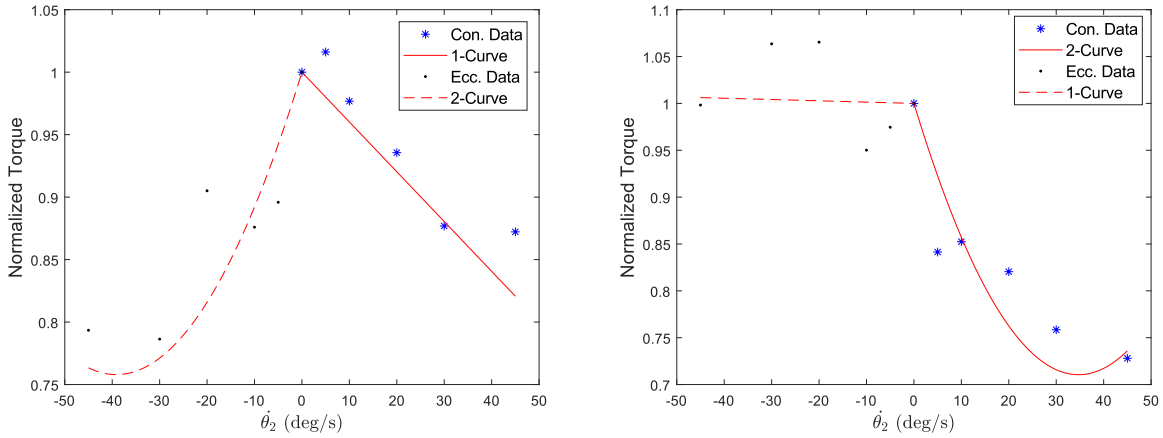

(a) Female General Model

(b) Male General Model

Figure 5.5: Comparison of the female general model and male general model for the torque-velocity scaling function in elevation ($\tau_{\omega_2}(\dot{\theta}_2)$).

the isometric measurements, and higher errors are more commonly observed in the torque-velocity scaling fits (particularly in eccentric motions) compared to the torque-angle scaling fits. The higher errors could be due to the intercept constraint that was used to avoid a discontinuity between concentric and eccentric curves, along with the fact that participants found the isokinetic testing more tiring compared to isometric testing.

For the passive torque functions, large RMSPEs are observed for the curve and surface fits compared to the torque-angle and torque-velocity scaling functions. One reason for the high errors is due to the nature of passive torques. As the passive torques are low in the ROM (8.3 Nm $\pm$ 0.15 Nm maximum in plane of elevation and 4.7 Nm $\pm$ 0.37 Nm maximum in elevation), a difference of a few Nm has a larger effect on the RMSPE compared to that of isometric measurements and isokinetic measurements. The accuracy of the Biodex could also contribute to the high errors seen for the passive torque functions, as the Biodex is accurate to 6.8 Nm, while the passive torques are often smaller. However, in terms of the overall model the passive torques are significantly smaller than the active torques and therefore the passive torques have a small impact on the overall model results.

For the passive functions with limited coupling ($\tau_{p_1}(\theta_1)$ and $\tau_{p_2}(\theta_2)$), 3-Curves were the best fit for all models. For the passive functions with coupling ($\tau_{p_1}(\theta_1, \theta_2)$ and $\tau_{p_2}(\theta_1, \theta_2)$), surfaces with 3 degrees are more common for θ_2 in elevation ($\tau_{p_2}(\theta_1, \theta_2)$). The cubic relationship results in an increase in passive torque towards the extreme ROMs, similar to that of the double exponential function that is commonly used for the passive scaling function.

The passive function with coupling for the plane of elevation torques ($\tau_{p_1}(\theta_1, \theta_2)$) results in 1 degree surfaces for θ_2 in the female and male general models and 2 degrees for θ_2 in the completely general model, indicating that elevation has a more linear impact on the torque in horizontal adduction motions. Figure 5.6 shows a comparison of the completely general model in plane of elevation and elevation for the coupled passive functions ($\tau_{p_1}(\theta_1, \theta_2)$ and $\tau_{p_2}(\theta_1, \theta_2)$).

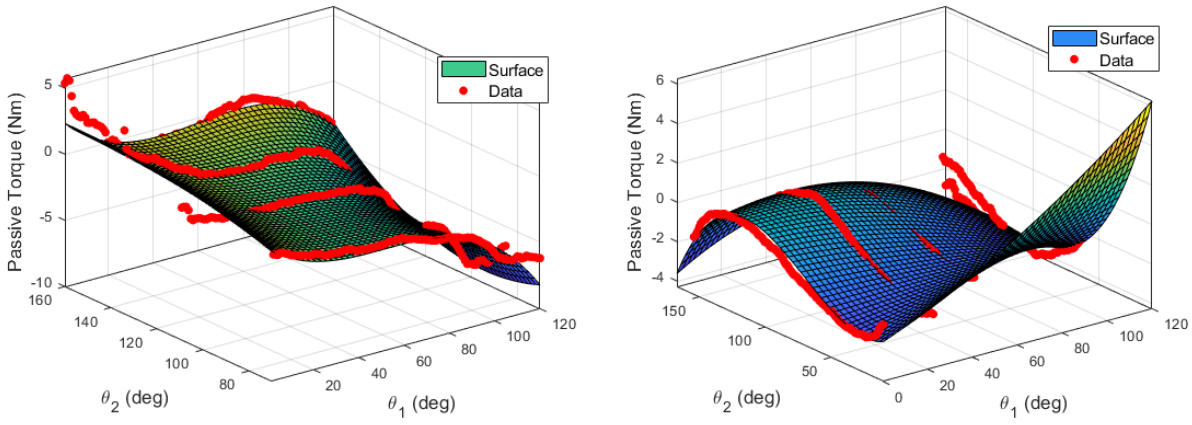

(a) Plane of Elevation Torques

(b) Elevation Torques

Figure 5.6: Comparison of the completely general model in plane of elevation and elevation for the coupled passive functions ($\tau_{p_1}(\theta_1, \theta_2)$ and $\tau_{p_2}(\theta_1, \theta_2)$).

On average, the completely general fits have a lower RMSPE than the male and female general fits. One reason for this could be due to the number of data points used for the models. For the completely general model for the elevation torques, the torque data for all 20 participants are averaged, while for the male and female models in elevation the data for 10 participants are averaged. For plane of elevation torques, the number of participants is reduced to 13 for the completely general model, 6 for the female general model, and 7 for the male general model. The larger number of participants may lead to a more visible trend in the completely general model fits compared to the other model types.

Subject-Specific Model Results

Curves and surfaces were fit to individual participants' data to create 13 subject-specific models. The average fit type, the average RMSPE, and the standard deviation of the error are presented in Table 5.3. Similar to the general models, A1 and A2 for the final eight

functions in the table indicate whether the first or second activation method was applied, and the passive torques were normalized by the absolute maximum passive torques to allow for the calculation of the RMSPE of the passive torques.

The first thing to note is that 3-Curves and 3,3-Surfaces were the average fit for all MTG functions except for the plane of elevation coupled torque-velocity scaling ($\tau_{\omega_1}(\dot{\theta_1}, \dot{\theta_2})$) in the eccentric case for activation method one and two, and the elevation coupled torque-velocity scaling ($\tau_{\omega_2}(\dot{\theta_1}, \dot{\theta_2})$) in the eccentric case for activation method two, which result in 3,2-Surfaces and a 2,3-Surface, respectively. The average RMSPE is also lower than that of the general models. The reason for the difference in errors between the general and subject-specific models could be due to the complex nature of the shoulder joint. As individual anatomy varies across the population, so does torque production and therefore it is harder to model the population compared to one individual [15]. However, there is a potential source of error for the subject-specific models. To prevent fatiguing of participants, each torque measurement was only collected once per participant. If a participant did not use their MVC, it is still reflected in the model as the maximum. The risk of this is reduced in the general models as k-fold cross validation was used for the participant group, finding a model that best fits more than one participant's results and therefore reducing the impact of an error in measurement. As higher-degree curves and surfaces were used to fit the subject-specific results compared to the general, there is also the risk that the curves and surfaces are overfitting the data, again since k-fold cross validation was not possible for these models.

Evaluating the average fits and variability in Table 5.3, the lowest variability on average is displayed in the torque-angle scaling functions for functions with ($\tau_{\theta_1}(\theta_1, \theta_2)$, $\tau_{\theta_2}(\theta_1, \theta_2)$) and without ($\tau_{\theta_1}(\theta_1)$, $\tau_{\theta_2}(\theta_2)$) coupling. As seen in the general models, there is also a higher average RMSPE for the eccentric fits compared to the concentric, with the highest error resulting from the torque-velocity scaling function for elevation torques in eccentric motion ($\tau_{\omega_2}(\dot{\theta_1}, \dot{\theta_2})$) with an average RMSPE of 11.6%. This could indicate that the activations calculated using the second method are not a reasonable assumption for the eccentric motion of all participants.

5.2 Model Validation

The general and subject-specific models were validated using isokinetic testing data where the angle and velocity dependencies were maintained (the regression process outlined in Chapter 4 was not completed to remove the angle dependencies). The isokinetic test was conducted at 5 deg/s with the Biodex dynamometer being tilted 30 degrees from the

Table 5.3: Subject-Specific Muscle Torque Generator Functions Average Fitting Results and Accuracy

Function	Average Fit Type	Average RMSPE	Standard Deviation
$\tau_{\theta_1}(\theta_1)$	3-Curve	2.9%	2.3%
$\tau_{\theta_2}(\theta_2)$	3-Curve	1.9%	1.9%
$\tau_{p_1}(\theta_1)$	3-Curve	7.3%	4.5%
$\tau_{p_2}(\theta_2)$	3-Curve	9.5%	3.3%
$\tau_{\omega_1}(\dot{\theta_1})$ Con.	3-Curve	7.4%	6.3%
$\tau_{\omega_1}(\dot{\theta_1})$ Ecc.	3-Curve	7.7%	6.4%
$\tau_{\omega_2}(\dot{\theta_2})$ Con.	3-Curve	6.3%	7.3%
$\tau_{\omega_2}(\dot{\theta_2})$ Ecc.	3-Curve	8.1%	7.2%
$\tau_{\theta_1}(\theta_1, \theta_2)$	3,3-Surface	6.4%	1.5%
$\tau_{\theta_2}(\theta_1, \theta_2)$	3,3-Surface	5.6%	2.4%
$\tau_{p_1}(\theta_1, \theta_2)$	3,3-Surface	9.7%	3.7%
$\tau_{p_2}(\theta_1, \theta_2)$	3,3-Surface	10.3%	3.8%
$\tau_{\omega_1}(\dot{\theta_1}, \dot{\theta_2})$ Con. A1	3,3-Surface	8.6%	5.2%
$\tau_{\omega_1}(\dot{\theta_1}, \dot{\theta_2})$ Ecc. A1	3,2-Surface	7.6%	3.8%
$\tau_{\omega_2}(\dot{\theta_1}, \dot{\theta_2})$ Con. A1	3,3-Surface	8.2%	4.5%
$\tau_{\omega_2}(\dot{\theta_1}, \dot{\theta_2})$ Ecc. A1	3,3-Surface	8.6%	4.2%
$\tau_{\omega_1}(\dot{\theta_1}, \dot{\theta_2})$ Con. A2	3,3-Surface	8.8%	1.6%
$\tau_{\omega_1}(\dot{\theta_1}, \dot{\theta_2})$ Ecc. A2	3,2-Surface	9.1%	4.1%
$\tau_{\omega_2}(\dot{\theta_1}, \dot{\theta_2})$ Con. A2	3,3-Surface	8.7%	3.7%
$\tau_{\omega_2}(\dot{\theta_1}, \dot{\theta_2})$ Ecc. A2	2,3-Surface	11.6%	6.8%

vertical (corresponding to an α of 60 degrees), resulting in a motion that used both plane of elevation and elevation torques. The best curve and surface fits were found for the 2 DOF MTG model, and the shoulder joint angles (θ_1, θ_2) and the shoulder joint angular velocities ($\dot{\theta_1}$, $\dot{\theta_2}$) from the resulting experimental motion were used as the inputs to the general and subject-specific models. While the Biodex limited the participant's angular velocity to 5 deg/s for the isokinetic test, no processing was done to remove torques that fell below this limit in order to observe the impact of angular velocity on the model.

5.2.1 General Models

For the general models, participant data was averaged for the isokinetic motion and the average experimental torque was compared against the model results. The completely general model, the female general model and the male general model were compared against the experimental results for the three coupling methods presented in Chapter 3 (Equations 3.1 to 3.6). The completely general model used all participant experimental data for comparison, while the female and male general models used experimental data averaged across the female and male participants, respectively. As two different activation assumptions were evaluated, the model validation was completed for both methods. The first activation method (A1) that assumes a sine and cosine relationship is evaluated first, followed by the second activation method (A2) where the independent activations were solved for directly.

First Activation Method (A1)

Table 5.4 presents the three general model's validation results for the total torque using the first activation method for the three different coupling methods. For the completely general model and the female model, the RMSEs and the RMSPEs increase with an increase in the coupling, with Method 3 (containing position and velocity coupling) resulting in the highest error for both models. In the male model, the position and velocity coupling case, Method 3, similarly results in the highest error as it did for the completely general and female general models. However, the lowest error is not seen in Method 1 and instead is observed in the position coupling case, Method 2. Comparing the three general models, Method 2 of the male general models presents the lowest error of 6.4%, while the lowest error in the female model is 17.5%. The completely general model results in errors between the female and male general models, with an error of 8.5%. The female model errors are significantly higher than the completely general and male general models. This could indicate that the first activation method is a good assumption for the completely general and male general models but is not a good assumption for the female general models. As

the passive torques are significantly smaller than the active torques scaled by the torque-angle and torque-velocity scaling functions, the model errors will be minimally affected by the passive torques. The average and standard deviation of the experimental data for the torque predicted by the three general models have been plotted against the three model methods to visually compare the errors in Figures 5.7-5.9.

Table 5.4: General Model Validation Results For Total Torque Using the First Activation Method A1

	All		Female		Male	
Method	RMSE (Nm)	RMSPE	RMSE (Nm)	RMSPE	RMSE (Nm)	RMSPE
1	3.5	8.5%	5.3	17.5%	3.9	7.6%
2	3.8	9.0%	6.0	20.0%	3.3	6.4%
3	4.7	11.3%	8.0	26.6%	5.0	9.7%

First, the completely general experimental torques are compared against the completely general model for Methods 1, 2 and 3 in Figure 5.7. The first half of the motion is concentric, and the second half is eccentric, resulting in negative torques due to the change of direction. There is a large standard deviation for the experimental torques because male isometric and isokinetic torques at the shoulder are on average higher than female torques [30], resulting in a greater spread of the data. The model tended to predict close to the mean experimental torques in concentric motions and overestimated compared to the mean experimental torques in eccentric motions. Method 1 shows the best estimation for concentric motion, with a slight overestimation of eccentric torques. The accuracy of the concentric prediction could be attributed to the torque-angle scaling functions of Method 1 ($\tau_{\theta_1}(\theta_1)$ and $\tau_{\theta_2}(\theta_2)$) resulting in the lower fitting errors compared to the coupled torque-angle scaling functions of Methods 2 and 3 ($\tau_{\theta_1}(\theta_1, \theta_2)$ and $\tau_{\theta_2}(\theta_1, \theta_2)$). As Method 2 has the same torque-velocity scaling function as Method 1, the impact of the coupled torque-angle scaling function is observed. For the completely general model, the coupled torque-angle scaling function results in a slight underestimation of the torque. Method 3 introduces the coupled torque-velocity scaling functions ($\tau_{\omega_1}(\dot{\theta}_1, \dot{\theta}_2)$ and $\tau_{\omega_2}(\dot{\theta}_1, \dot{\theta}_2)$. In concentric motions, the impact of the coupled torque-velocity scaling function results in an underestimation of the torque, indicating that the torque is reduced too much. However, in eccentric motions the coupled torque-velocity scaling performs better than the uncoupled torque-velocity scaling, reducing the overestimation of the eccentric torques.

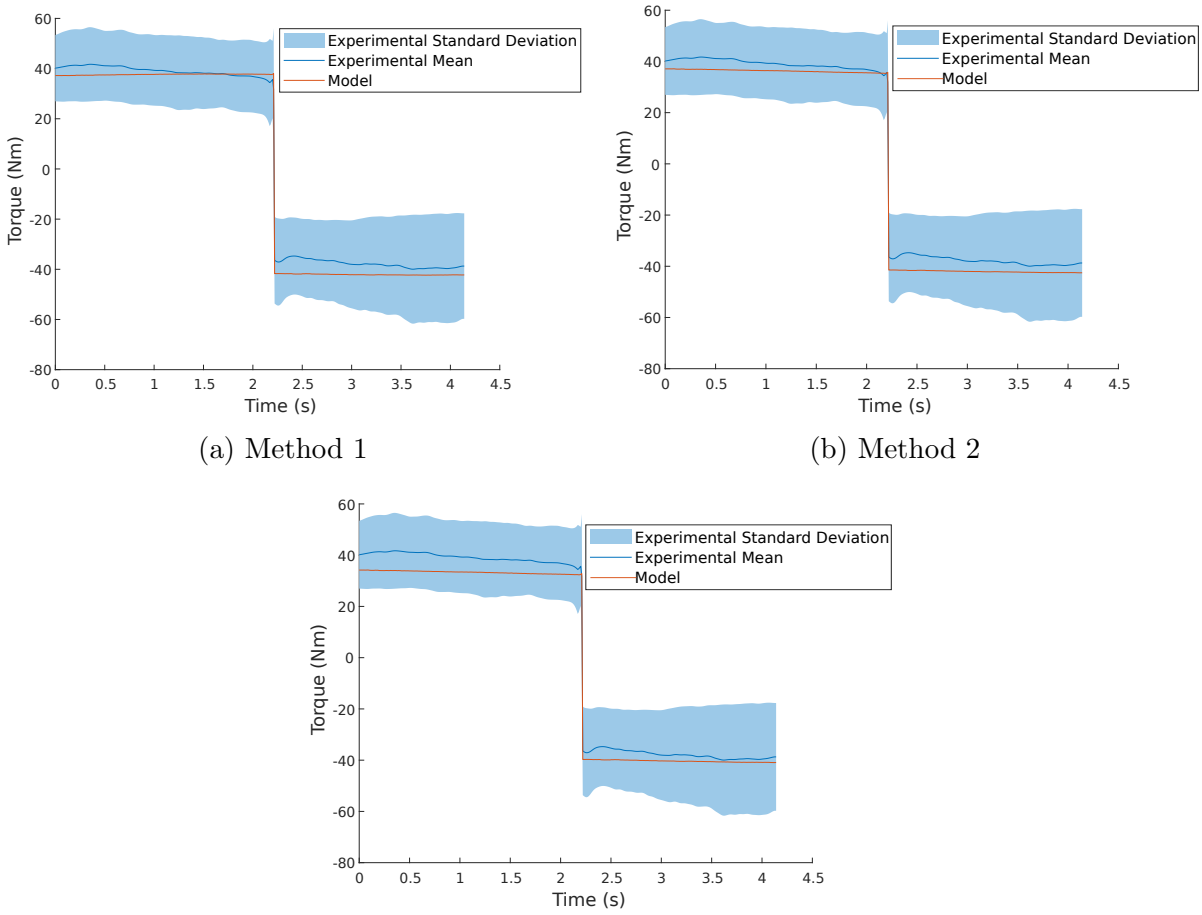

(a) Method 1

(b) Method 2

(c) Method 3

Figure 5.7: Torque results of the completely general model for Method 1, 2, and 3 using the first activation method compared against experimental torque data averages across all participants.

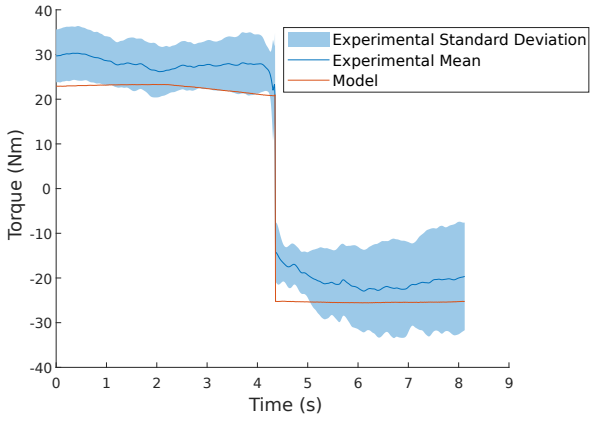

(a) Method 1

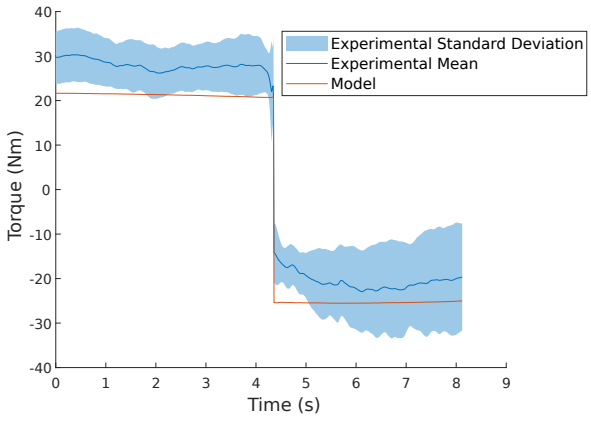

(b) Method 2

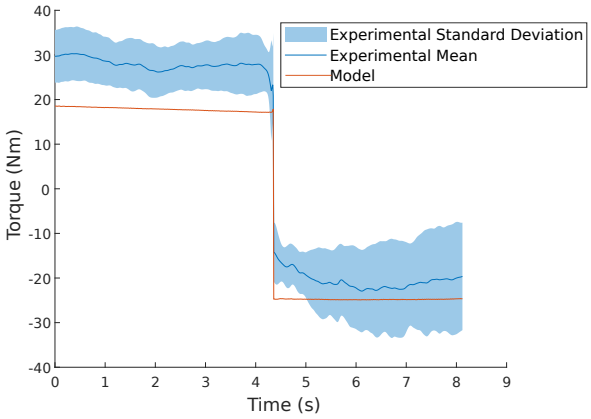

(c) Method 3

Figure 5.8: Torque results of the female general model for Method 1, 2, and 3 using the first activation method compared against experimental torque data averages across all female participants.

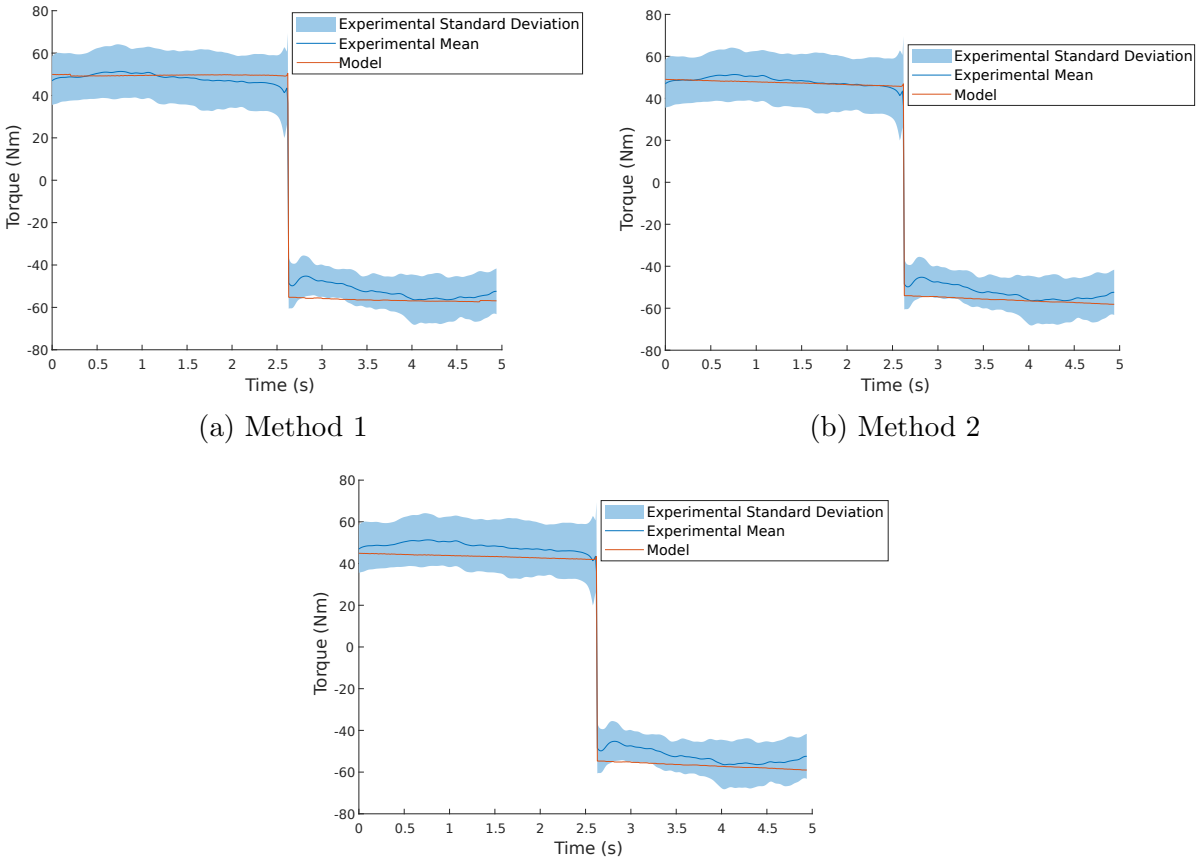

(a) Method 1

(b) Method 2

(c) Method 3

Figure 5.9: Torque results of the male general model for Method 1, 2, and 3 using the first activation method compared against experimental torque data averages across all male participants.

Figure 5.8 presents the results for the female general model for Methods 1, 2 and 3 compared against the experimental average torque data for the participant subset. The model shows a poor estimation for concentric torques across all methods, with the concentric torques being the best represented in Method 1. As seen in Method 2, the coupled torque-angle scaling functions ($\tau_{\theta_1}(\theta_1, \theta_2)$ and $\tau_{\theta_2}(\theta_1, \theta_2)$) resulted in a greater underestimation of the torques in concentric motion. The velocity coupling in Method 3 results in the highest underestimation of torques in concentric motion, indicating that the velocity coupling case is scaling the torques more aggressively than what is physically occurring. One thing to note is the large spread of experimental data at the end of the eccentric motion. This could indicate that certain participants were fatigued and were no longer using their maximum torque, while other participants were not yet experiencing fatigue. The model is operating under the assumption that MVC is used, and the first activation method assumes that the concentric and eccentric torques have the same activation, and therefore this could explain why the experimental eccentric torques are lower than that of the model. The injury prevention mechanism outlined by [73] could also account for lower muscle activation seen in experimental eccentric torques. As the errors are high across all methods for the female general model, the first activation method is not a good approach for the female population. As previously mentioned, women typically show more muscle activation in muscles outside of the primary loading direction [2]. As the isokinetic motion tested is primarily in elevation, higher plane of elevation activations could result in a more accurate activation representation.

Finally, the results of the male general model for Methods 1, 2 and 3 are compared against the average experimental torque data across the male participants in Figure 5.9. The male general model shows a good estimation of concentric torques for Methods 1 and 2, with Method 2 resulting in the lowest RMSPE out of the three proposed methods. Method 3, which introduces the velocity coupling, results in an underestimation of the concentric torques, indicating that the coupled torque-velocity scaling functions scale the torques more aggressively than what is physically occurring for the completely general, the female general and the male general models. Again, similar to the female general model, fatigue and the injury prevention mechanism may be preventing the participant from using their MVC in the experiments, while the model is assuming MVC and therefore predicts a higher torque for eccentric motions. However, less of an overestimation in eccentric torques is seen in the male general model compared to the female general, which could be due to the male participants producing more consistent eccentric torques (seen through the consistency in the standard deviation). The male general model also resulted in the lower errors compared to the completely general and female general models, showing that the first activation method is more applicable to the male general model.

Second Activation Method (A2)

Table 5.5 presents the three general model's validation results using the second activation method for the three different coupling methods. For the female model, the RMSEs and the RMSPEs increase with an increase in the coupling, with Method 3 containing position and velocity coupling resulting in the highest error. For the completely general model, the position and velocity coupling case, Method 3, similarly results in the highest error as it did for the female general model; however, the lowest error is observed in the position coupling case, Method 2. For the male general model, the highest error is found using Method 1 which had limited coupling, followed by Method 3, with Method 2 resulting in the lowest error. Comparing the three general models, Method 2 of the completely general model presents the lowest error of 8.0%, while the lowest error of the female model is 11.6%. The lowest error of the male model was obtained using Method 2, which resulted in an error of 12.7%. Compared to the first activation method, all errors increased except for the completely general model's Method 2, and the female general model's Methods 1 and 2 where the errors decreased. The average and standard deviation of the experimental data for the three general models have been plotted against the three model methods in order to visually compare the errors in Figures 5.10-5.12.

Table 5.5: General Model Validation Results For Total Torque Using the Second Activation Method A2

	All		Female		Male	
Method	RMSE (Nm)	RMSPE	RMSE (Nm)	RMSPE	RMSE (Nm)	RMSPE
1	4.5	10.8%	3.5	11.6%	8.6	16.8%
2	3.1	8.0%	3.8	12.5%	6.5	12.7%
3	5.2	12.4%	9.4	31.1%	7.4	14.4%

First, the completely general experimental torques were compared against the completely general model for Methods 1, 2 and 3 using the second activation method in Figure 5.10. All three methods estimate the model torques to be very similar to the experimental mean, resulting in a better estimate for eccentric torques compared to those estimated using the first activation method. The second activation method used separate activations for concentric and eccentric motions in order to account for any reduction in eccentric

motions, while the first activation method did not consider this. Therefore, different activations for concentric and eccentric motions produced more accurate eccentric torques for the completely general model. Comparing Methods 1 and 2 of the completely general model, it is seen that the coupled torque-angle scaling function in Method 2 resulted in less overestimation of concentric torque. Method 3, which introduced the coupled torque-velocity scaling functions ($\tau_{\omega_1}(\dot{\theta}_1, \dot{\theta}_2)$ and $\tau_{\omega_2}(\dot{\theta}_1, \dot{\theta}_2)$), resulted in a similar underestimation of torques when compared to the Method 3 of the first activation method.

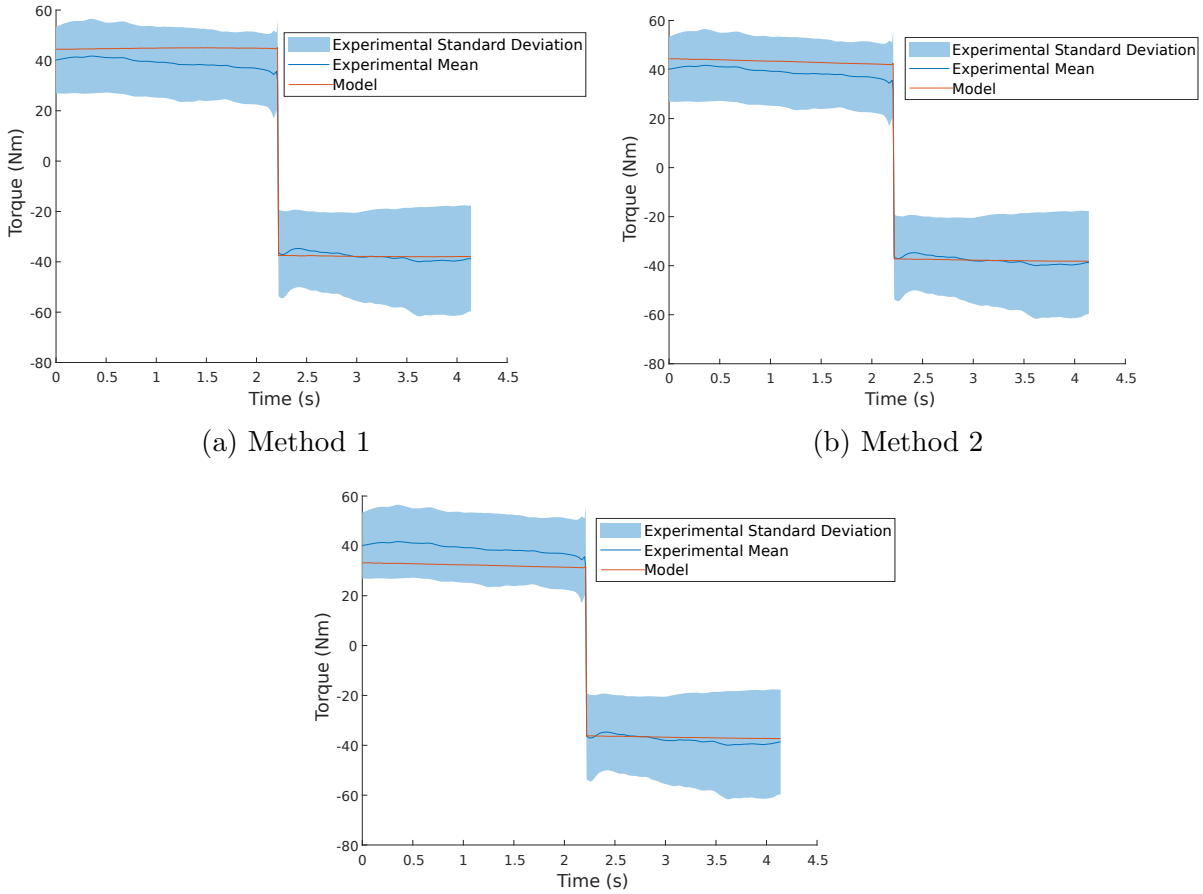

(a) Method 1

(b) Method 2

(c) Method 3

Figure 5.10: Torque results of the completely general model for Method 1, 2, and 3 using the second activation method compared against experimental torque data averages across all participants.

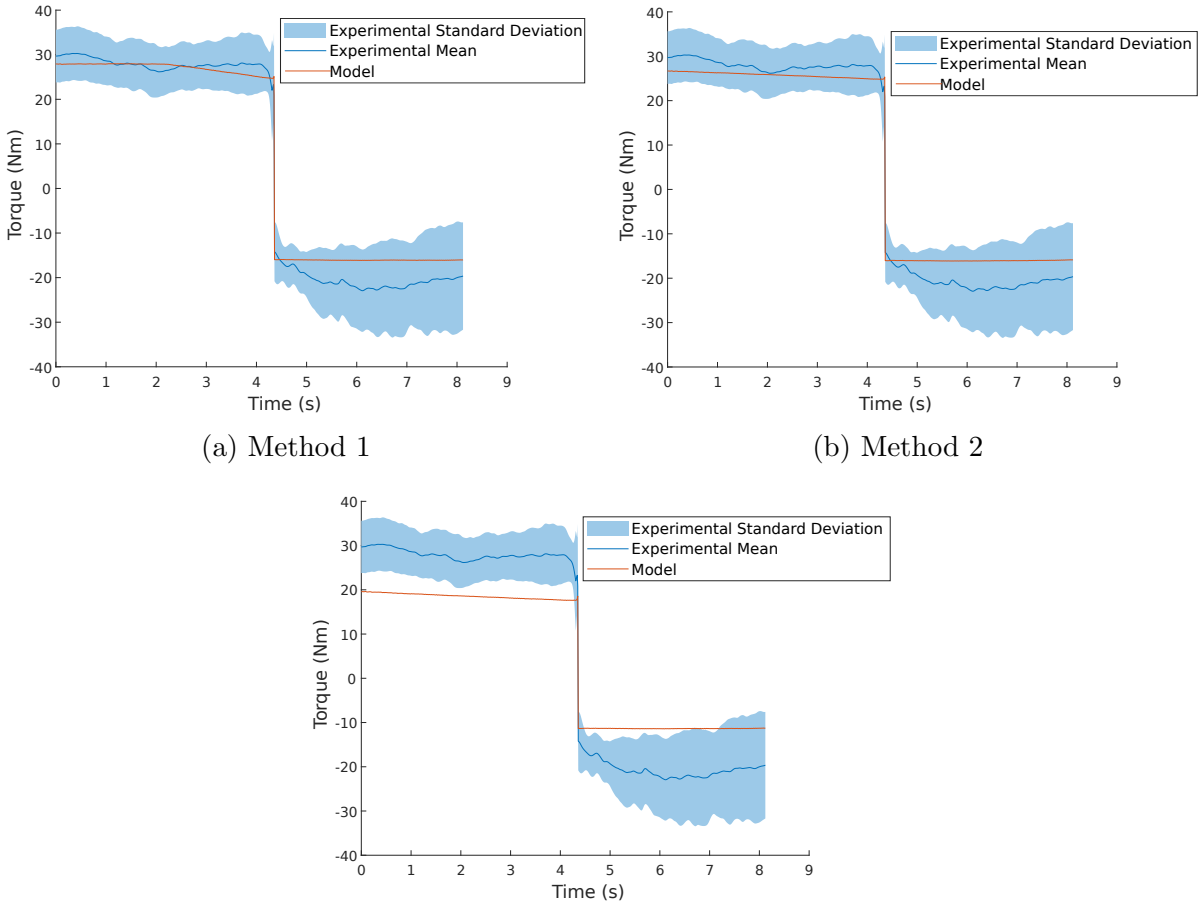

(a) Method 1

(b) Method 2

(c) Method 3

Figure 5.11: Torque results of the female general model for Method 1, 2, and 3 using the second activation method compared against experimental torque data averages across all female participants.

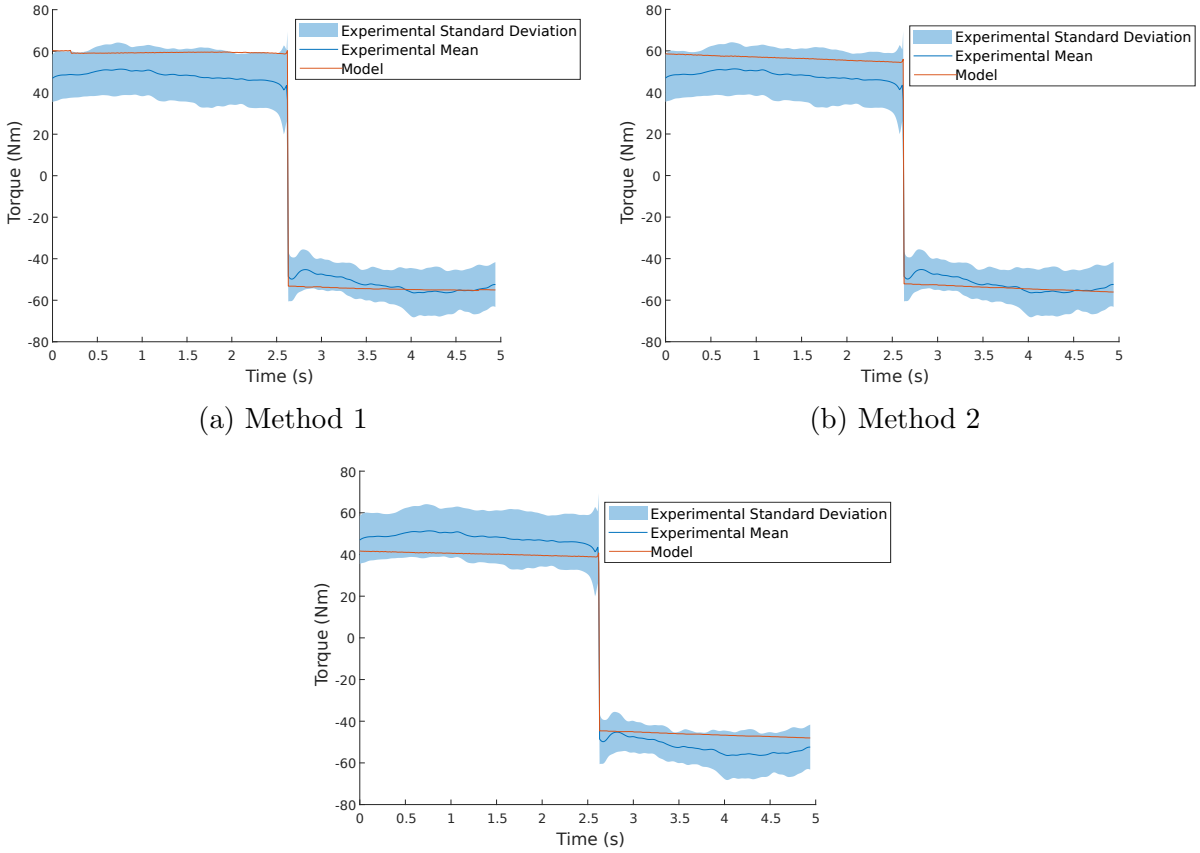

(a) Method 1

(b) Method 2

(c) Method 3

Figure 5.12: Torque results of the male general model for Method 1, 2, and 3 using the second activation method compared against experimental torque data averages across all male participants.

Figure 5.11 shows the results for the female general model for Methods 1, 2 and 3 using the second activation method compared against the experimental average torque data for the participant subset. Method 1 resulted in estimated concentric torques that were the most similar to the experimental mean, with the coupled torque-angle scaling in Method 2 resulting in a slight underestimation. Compared to the first activation method, which resulted in a torque estimation at the lower end of the standard deviation, the second activation method performed better. For the female model using the second activation method, a_1 and a_2 were both determined to be 1 when α was 60 degrees for concentric motion, resulting in higher activations compared to the first activation method. These higher activations resulted in concentric torque estimations closer to the experimental mean. Method 3 resulted in underestimation of both the concentric and eccentric torques. As the activations are considered in Method 3, the high activations determined resulted in a more significant torque scaling for the coupled torque-velocity scaling function, and therefore produced less accurate results when compared to the experimental torque data.

Finally, the results of the male general model for Methods 1, 2 and 3 using the second activation method are compared against the average experimental torque data across the male participants in Figure 5.12. The higher concentric activations that were determined for the second activation method compared to the first resulted in an overestimation for both Method 1 and 2, suggesting that the first activation method is a better approach for a general male model. The lower activations for eccentric motion provide a torque estimate slightly closer to the experimental mean, again supporting the benefit of separate concentric and eccentric activations. Lastly, the coupled torque-velocity scaling used in Method 3 resulted in underestimations of torques similar to the other general model types.

Overall, general torque data that is a function of two angles and two angular velocities can be modeled for the shoulder using a 2 DOF MTG. For the general models, two different activation methods were considered along with the degree of coupling. The second activation method provided the best results for both the completely general model and the female general model, with Method 2 providing the lowest error for the completely general model (RMSPE of 8.0%) and Method 1 providing the lowest error for the female general model (11.6%). The first activation method was a better approach for the male general model, with Method 2 providing the lowest error of 6.4%. The methods that resulted in the lowest errors for the models all had RMSEs lower than the accuracy of the Biodex. It was noted that for the general models, separate concentric and eccentric activations provided a better estimate for the torques compared to the same activation used for concentric and eccentric motions. Method 3 that used the coupled torque-velocity scaling also resulted in a scaling that was too aggressive for the general models. This could be due to the isokinetic testing used for the functions, as participants were instructed to use their MVC

many times for this study. With an increase in MVCs, there is an increased risk of fatigue which would result in lower torque production and therefore more aggressive scaling in the coupled torque-velocity scaling function. The MTG function parameters for the general models that resulted in the lowest validation errors are listed in Appendix B.

5.2.2 Subject-Specific Models

For the subject-specific models, individual participant torques for the isokinetic motion were compared against a subject's model results for the three coupling equations presented in Chapter 3. Again, as two activation methods were considered, the model validation was completed for both methods.

First Activation Method (A1)

Table 5.6: Average Subject-Specific Model Validation Results For Total Torque Using the First Activation Method A1

Method	Average RMSPE	Standard Deviation
1	24.1%	11.6%
2	23.1%	11.5%
3	22.8%	12.2%

Table 5.6 presents the average of the 13 subject-specific models using the first activation method for the three coupling methods as well as the standard deviation. For the subject-specific models, an increase in coupling resulted in a decrease in the average model error, with Method 1 having the highest error of 24.1% and Method 3 with the lowest of 22.8%. Method 3 producing the lowest error conflicts with the results from the general models, as Method 3 resulted in the highest error for the general models. It is more difficult to capture a general population trend compared to a subject-specific trend [15], so it is likely that the subject-specific models were able to determine a more accurate coupled torque-velocity scaling function compared to the general models. However, Method 3 does result in the highest standard deviation of the methods. As many participants found the isokinetic testing difficult, the coupled torque-velocity scaling functions could have

been fit to experimental results that did not best represent the true participant torque-velocity scaling function for some participants, leading to a higher deviation for Method 3. If participants repeated the isokinetic testing and an average result was found, a torque-velocity scaling function that was more representative of the participant might be obtained. The high standard deviations for all models indicate that some subject-specific models fit with higher accuracy than others. The large variability in accuracy again could be attributed to the subject-specific models being based on experimental results that were not repeated.

Figure 5.13 shows an example of a subject-specific model for the three coupling methods for one participant. While the 2 DOF MTG is unable to predict the chatter produced from the experimental torque, all three models predict the general trend, which may be sufficient for a forward dynamic simulation. Method 3 results in a better estimation of the eccentric torque data compared to Method 1 and 2, while Method 1 provides a more jagged result due to the linear interpolation used between fitted curves.

Second Activation Method (A2)

Table 5.7 presents the average of the 13 subject-specific models using the second activation method for the three coupling methods as well as the standard deviation. Similar to the first activation method, the highest error is seen with the least amount of coupling; however, using the second activation method, Method 2 results in the lowest error instead of Method 3. As Method 3 used the activation when determining the coupled torque-velocity scaling function, it is possible that the activation method does not represent what is physically occurring for some participants, or that not enough data points were used when determining the activations.

Table 5.7: Average Subject-Specific Model Validation Results For Total Torque Using the Second Activation Method A2

Method	Average RMSPE	Standard Deviation
1	25.3%	13.1%
2	23.0%	12.9%
3	24.4%	12.5%

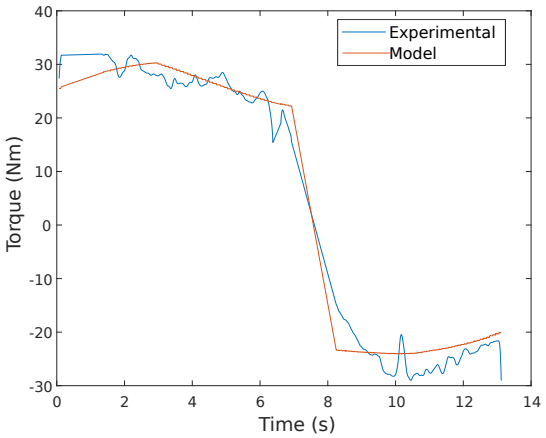

(a) Method 1

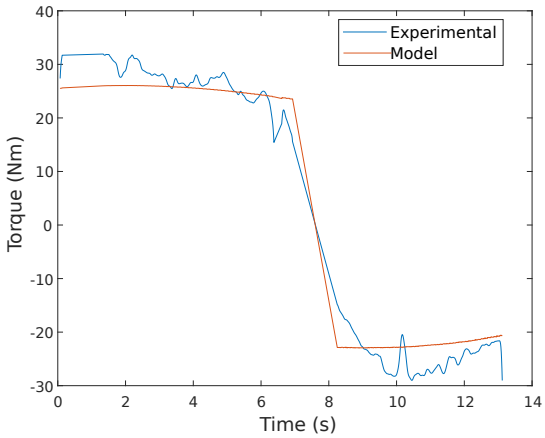

(b) Method 2

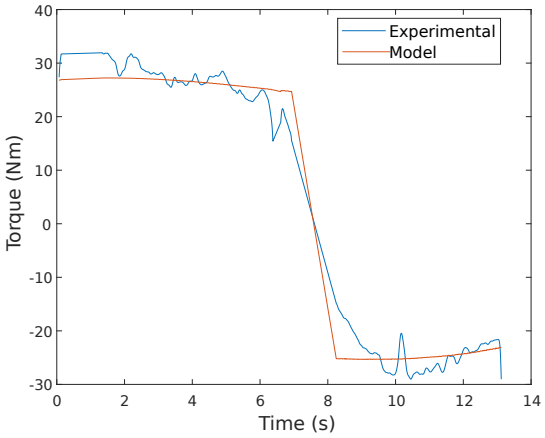

(c) Method 3

Figure 5.13: Torque results of the subject-specific model of one participant using the first activation method for Methods 1, 2, and 3 compared against the experimental torque data of the participant.

When comparing the validation results of the general models (see Tables 5.4 and 5.5) against the subject-specific results (Tables 5.6 and 5.7), it can be seen that the subject-specific models result in a higher error when compared to the general models. This is opposite to the fitting results, where for the general models (Table 5.2) a higher fitting error is seen compared to the subject-specific models (Table 5.3). The general fitting errors are higher than the subject-specific fitting errors as the general model uses k-fold cross validation to determine the best fit to more than one individual's torque data. As the population has differences in shoulder anatomy, it is difficult to accurately represent a group [15], and therefore we see higher errors compared to subject-specific models that are fit to one participant. When validating, the general models are validated against a population's averaged torque results, while the subject-specific models results are validated against a single participant's torque results, which has more noise compared to the averaged data. The noise in the subject-specific data could be contributing to the higher validation errors. The general data also uses k-fold cross validation to find functions that best fit the average population, and therefore we see low fitting errors to the average population torque data. The subject-specific model validation has a larger range of fitting results, which could be attributed to some participants not using their MVC during a motion, resulting in an inaccurate model and higher average validation errors. In the future, collecting and averaging multiple subject-specific trials would reduce noise and could lead to lower validation errors.

Figure 5.14 shows an example of a subject-specific model using the second activation method for the three coupling methods for one participant. Methods 1 and 2 both result in the eccentric torques being underestimated for the participant, while Method 3 provides the best estimate for the particular participant even though it was not the best method for all participants. This again highlights how some subject-specific models fit with higher accuracy compared to others.

Overall, subject-specific data that is a function of two angles and two angular velocities can be modeled using a subject-specific 2 DOF MTG model. The first activation method resulted in lower errors compared to the second, with the model accuracy increasing with an increase in coupling. The lowest average error was for Method 3 and was 22.8%. Altogether, the results of these models are highly dependent on the participant using their MVC throughout the entire study, as measurements were not repeated. Therefore, some of the subject-specific models perform better than others, and on average have a lower accuracy compared to the general models.

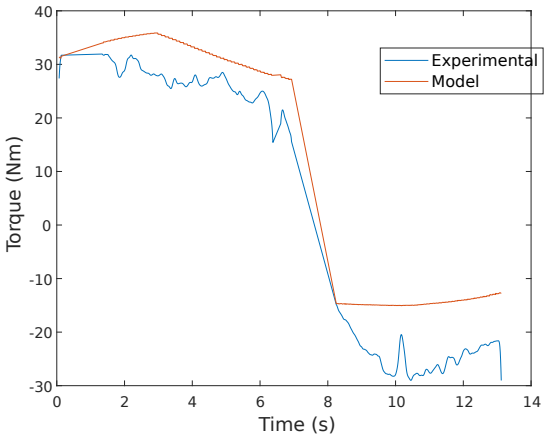

(a) Method 1

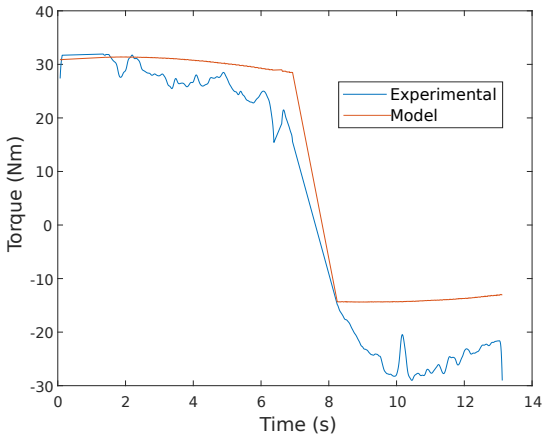

(b) Method 2

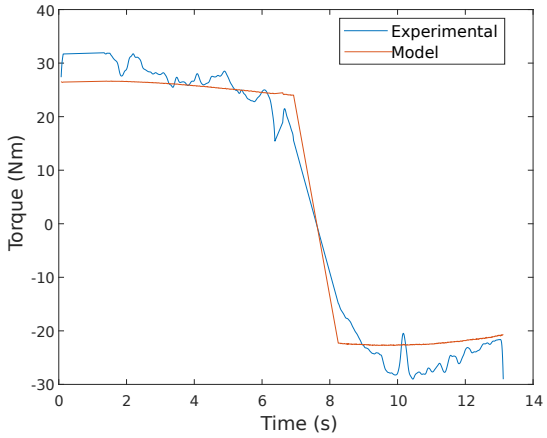

(c) Method 3

Figure 5.14: Torque results of the subject-specific model of one participant using the second activation method for Methods 1, 2, and 3 compared against the experimental torque data of the participant.

Chapter 6

Conclusion

In this chapter, the research is summarized and the limitations of the study are discussed. Recommendations for future work in this area of research are also proposed.

6.1 Research Summary

Work in the field of muscle modeling has led to the innovation of MTGs, a model that reduces the complexity of muscle-force models to a single torque at the joint, allowing for faster forward dynamic simulations. However, there is a lack of MTG models that accounts for coupling between 2 DOF at a joint, leading to complexity in modeling three-dimensional joint motion for complicated joints such as the shoulder. This was motivation to develop multi-DOF MTGs as a function of two angles and angular velocities at the shoulder joint. A background understanding of the previous structure of single DOF MTGs was presented in Chapter 2 and was used to develop different 2 DOF MTG models that represented different degrees of coupling between the two joint angles and angular velocities. The research was completed with the development of subject-specific and general 2 DOF MTG models for the different degrees of coupling for the first time, comparing the effect that coupling has on the model accuracy.

Multi-Degree-of-Freedom Muscle Torque Generator Model

In Chapter 3, the definitions for the multi-DOF MTG were outlined. The different coupling equations were developed and presented for elevation and plane of elevation torques.

The equations for the torque-angle and torque-velocity scaling functions as well as the passive and activation functions were outlined. The torque-angle scaling, the torque-velocity scaling and passive functions were designed to be polynomial curves and surfaces whose fit was evaluated up to 3 degrees.

Shoulder Experiments

Experimental torque data was gathered to fit the subject-specific and general MTG functions in Chapter 4. Dynamometry was used to collect isometric and passive elevation torques as a function of two angles, as well as the isometric and passive plane of elevation torques. Isokinetic testing was also conducted as a function of two joint angular velocities. The data was then processed to determine the maximum torque a participant could output at the test points outlined.

Multi-Degree-of-Freedom Muscle Torque Generator Model Fitting and Comparison

In Chapter 5, the experimental data collected was used to fit curves and surfaces to the MTG functions for subject-specific and general models. Three general models were evaluated, a completely general model, a female general model and a male general model. The fit type results were presented for the general models, as well as the average fit type for the subject-specific models. The models were finally validated using experimental data, and it was determined that for the general models, position coupling provided the best estimate of average joint torque for the completely general population and the male general population, while limited coupling provided the best estimate for the female population. For subject-specific models, position and velocity coupling provided the lowest error on average; however, the lack of repeated tests for the subject-specific models could be leading to inaccuracy in the velocity-coupling methods.

6.2 Limitations

- While participants were encouraged to use their MVC, it is possible that participants were not able to maintain their maximum for the full study. Participants might have experienced muscle fatigue or suppressed muscle activation in eccentric motions as a means of injury prevention [73]. Participants not using their MVC can lead to

inaccuracies in parameter fitting for the MTG functions. Testing subjects with the addition of EMG data would provide insight into the total muscle activation during the study [10].

- The 2 DOF MTG assumes that all the muscles at the shoulder joint are mono-articular, while in actuality the biceps brachii is a bi-articular muscle that spans both the shoulder and the elbow, and therefore torque production is not only affected by the shoulder joint angles but also that of the elbow [42]. MTG models that consider the bi-articular nature of muscles have previously been shown to be a better representation of human motion [43], and therefore the 2 DOF shoulder MTG could provide a better torque estimation if the effects of the elbow joint angle are considered.

- MTGs by nature make simplifications for faster simulations compared to muscle-force models. However, this leads to some drawbacks if the model aims to gain insight into certain elements of the human body. For example, as individual muscle fibers are not modeled, the force in these muscle fibers cannot be discerned [51]. Due to the simplicity of the MTG, bone-on-bone contact forces are also not able to be modeled. The agonist and antagonist co-contractions from muscles are also not individually accounted for in an MTG model, as the MTG provides only the net torque at the joint [20].

- Polynomial curves and surfaces were used for the torque-angle scaling, torque-velocity scaling, and passive functions of the 2 DOF MTG. While this leads to simple parameter fitting, the parameters do not have a physical meaning. Previous models have considered parameters with physical meaning, such as the torque-angle scaling functions by Anderson *et al.* [3] and Haering *et al.* [23], which use the angle that produces maximum torque and the ROM as parameters for the model. Adding parameters with physical meaning could improve the 2 DOF model's interpretability. Examining the physical meaning of the parameters could also provide additional insight when considering how to approach torques with different levels of activation.

- While the piecewise function used for the torque-velocity scaling function ensures a better fit for both concentric and eccentric motions, it has only C^0 continuity. This has a drawback that there is no derivative for optimization.

- Twenty participants has previously been found to be statistically significant for determining isometric and isokinetic strength [56]. However, this work applied 36 different curve and surface fits to the data from twenty participants. Increasing the number of participants would increase the statistical significance of the curve and surface fitting results.

6.3 Recommendations and Future Work

- The addition of a fatigue model, such as in [45], could be applied to the experimental data collected in order to account for the participant's fatigue over time.
- To increase the validity of subject-specific models, participants could return to the study on multiple days to repeat the protocol (randomizing the order of tests to reduce the impact of fatigue). The impact of less than maximum contractions would be reduced and a more robust subject-specific model could be created. EMG data collection could also be used to supplement the collected torque data, indicating the strength of participants' contractions.
- To increase the accuracy of the activation function, EMG data could be collected to compare the activation of muscles in the plane of elevation and elevation. Therefore, the experimental EMG data could be used for the muscle activation in place of the two activation assumptions made in this work.
- To increase the accuracy of the coupled torque-velocity scaling function, additional isometric measurements could be made in the same directions as the isokinetic testing. In this work, isometric tests were only conducted in the plane of elevation and elevation, meaning that isokinetic tests done outside of these motions needed to be decomposed into components in order to normalize the torque data for the scaling function. This also required the activations to be considered so that MVCs were compared. A simpler method would be to measure isometric torques in the direction of the isokinetic tests so that normalization could be done directly.
- The bi-articular effects of the biceps brachii could be modeled to increase the fidelity of the model [43]. As the shoulder torques were studied while the elbow was kept in a straight locked position, an additional study could be conducted to determine how elbow angle has an impact on the shoulder torque.
- While a 2 DOF model has been created for the shoulder, the shoulder has 3 DOF in total, and the effects of internal and external rotation were not considered. Additional data could be collected to expand the current model and add in the coupling effects of the final DOF for the shoulder.
- The current model studied a ROM and isokinetic speeds that were appropriate for lifting and reaching motions. To apply this model to other simulations, specifically those which are used in sports engineering, a larger ROM and faster speeds could be studied to expand the model's usability.

References

[1] R. Alexander. Optimum Take-Off Techniques for High and Long Jumps. *Philosophical Transactions: Biological Sciences*, 329(1252):3–10, 1990.

[2] C. Anders, S. Bretschneider, A. Bernsdorf, K. Erler, and W. Schneider. Activation of shoulder muscles in healthy men and women under isometric conditions. *Journal of Electromyography and Kinesiology*, 14(6):699–707, 12 2004.

[3] D. E. Anderson, M. L. Madigan, and M. A. Nussbaum. Maximum voluntary joint torque as a function of joint angle and angular velocity: Model development and application to the lower limb. *Journal of Biomechanics*, 40(14):3105–3113, 2007.

[4] M. Audu and D. T. Davy. The Influence of Muscle Model Complexity in Musculoskeletal Motion Modeling. *Journal of Biomechanical Engineering*, 107(2):147–157, 1985.

[5] C. Brown. Predictive forward dynamic simulation of manual wheelchair propulsion, 2018.

[6] C. Brown and J. McPhee. Predictive Forward Dynamic Simulation of Manual Wheelchair Propulsion on a Rolling Dynamometer. *Journal of Biomechanical Engineering*, 142(7), 4 2020.

[7] J. H. Buffi, K. Werner, T. Kepple, and W. M. Murray. Computing muscle, ligament, and osseous contributions to the elbow varus moment during baseball pitching. *Annals of Biomedical Engineering*, 43(2):404–415, 2015.

[8] H. C. Chong, L. M. Tennant, D. C. Kingston, and S. M. Acker. Knee joint moments during high flexion movements: Timing of peak moments and the effect of safety footwear. *The Knee*, 24(2):271–279, 2017.

[9] J. W. Chow, W. G. Darling, J. G. Hay, and J. G. Andrews. Determining the Force-Length-Velocity Relations of the Quadriceps Muscles: III. A Pilot Study. *Journal of Applied Biomechanics*, 15(2):200 – 209, 1999.

[10] M. Cifrek, V. Medved, S. Tonković, and S. Ostojić. Surface EMG based muscle fatigue evaluation in biomechanics. *Clinical Biomechanics*, 24(4):327–340, 5 2009.

[11] D. J. Cleather and A. M. J. Bull. Lower-extremity musculoskeletal geometry affects the calculation of patellofemoral forces in vertical jumping and weightlifting. *Proceedings of the Institution of Mechanical Engineers, Part H: Journal of Engineering in Medicine*, 224(9):1073–1083, 2010.

[12] F. De Groote, A. L. Kinney, A.V. Rao, and B. J. Fregly. Evaluation of direct collocation optimal control problem formulations for solving the muscle redundancy problem. *Annals of Biomedical Engineering*, 44(10):2922–2936, 2016.

[13] P. De Leva. Joint center longitudinal positions computed from a selected subset of Chandler's data. *Journal of Biomechanics*, 29(9):1231–1233, 1996.

[14] S. Delp, F. Anderson, A. Arnold, P. Loan, A. Habib, C. John, E. Guendelman, and D. Thelen. OpenSim: Open-Source Software to Create and Analyze Dynamic Simulations of Movement. *Biomedical Engineering, IEEE Transactions on*, 54:1940 – 1950, 10 2007.

[15] C. R. Dickerson, R. E. Hughes, and D. B. Chaffin. Experimental evaluation of a computational shoulder musculoskeletal model. *Clinical Biomechanics*, 23(7):886–894, 8 2008.

[16] G. A. Dudley, R. T. Harris, M. R. Duvoisin, B. M. Hather, and P. Buchanan. Effect of voluntary vs. artificial activation on the relationship of muscle torque to speed. *Journal of Applied Physiology*, 69(6):2215–2221, 1990.

[17] K. A. Edman. Double-hyperbolic force-velocity relation in frog muscle fibres. *The Journal of Physiology*, 404(1):301–321, 1988.

[18] M. Ezati. *Predictive Dynamic Simulation of Child Gait Using Direct Collocation Optimal Control*. PhD thesis, University of Waterloo, 2021.

[19] M. Febrer-Nafría, R. Pallarès-López, B. J. Fregly, and J. M. Font-Llagunes. Comparison of different optimal control formulations for generating dynamically consistent crutch walking simulations using a torque-driven model. *Mechanism and Machine Theory*, 154:104031, 2020.

[20] S. E. Forrester, M. R. Yeadon, M. A. King, and M. T. G. Pain. Comparing different approaches for determining joint torque parameters from isovelocity dynamometer measurements. *Journal of Biomechanics*, 44(5):955–961, 2011.

[21] E. A. Froese and M. E. Houston. Torque-velocity characteristics and muscle fiber type in human vastus lateralis. *Journal of Applied Physiology*, 59(2):309–314, 1985.

[22] A. M. Gordon, A. F. Huxley, and F. J. Julian. The variation in isometric tension with sarcomere length in vertebrate muscle fibres. *The Journal of Physiology*, 184(1):170–192, 1966.

[23] D. Haering, C. Pontonnier, N. Bideau, G. Nicolas, and G. Dumont. Using Torque-Angle and Torque–Velocity Models to Characterize Elbow Mechanical Function: Modeling and Applied Aspects. *Journal of Biomechanical Engineering*, 141(8), 5 2019.

[24] D. Haering, C. Pontonnier, and G. Dumont. Which mathematical model best fit the maximal isometric torque-angle relationship of the elbow? *Computer Methods in Biomechanics and Biomedical Engineering*, 20(sup1):S101–S102, 10 2017.

[25] J.D. Harry, A.W. Ward, N.C. Heglund, D.L. Morgan, and T.A. McMahon. Cross-bridge cycling theories cannot explain high-speed lengthening behavior in frog muscle. *Biophysical Journal*, 57(2):201–208, 1990.

[26] H. Hatze. A myocybernetic control model of skeletal muscle. *Biological Cybernetics*, 25(2):103–119, 1977.

[27] W. Herzog. The relation between the resultant moments at a joint and the moments measured by an isokinetic dynamometer. *Journal of Biomechanics*, 21(1):5–12, 1 1988.

[28] A. V. Hill. The heat of shortening and the dynamic constants of muscle. *Proceedings of the Royal Society of London. Series B-Biological Sciences*, 126(843):136–195, 1938.

[29] P.D. Hoang, R.B. Gorman, G. Todd, S.C. Gandevia, and R.D. Herbert. A new method for measuring passive length–tension properties of human gastrocnemius muscle in vivo. *Journal of Biomechanics*, 38(6):1333–1341, 2005.

[30] R. E. Hughes, M. E. Johnson, S. W. O'Driscoll, and K. An. Age-Related Changes in Normal Isometric Shoulder Strength. *The American Journal of Sports Medicine*, 27(5):651–657, 1999.

[31] K. A. Inkol, C. Brown, W. McNally, C. Jansen, and J. McPhee. Muscle torque generators in multibody dynamic simulations of optimal sports performance. *Multibody System Dynamics*, 50(4):435–452, 2020.

[32] R. Jacobs, M. F. Bobbert, and G. J. van Ingen Schenau. Mechanical output from individual muscles during explosive leg extensions: The role of biarticular muscles. *Journal of Biomechanics*, 29(4):513–523, 4 1996.

[33] C. Jansen and J. McPhee. Predictive dynamic simulation of Olympic track cycling standing start using direct collocation optimal control. *Multibody System Dynamics*, 49(1):53–70, 2020.

[34] Y. Jiang, T. Van Wouwe, F. De Groote, and C. K. Liu. Synthesis of biologically realistic human motion using joint torque actuation. *ACM Transactions on Graphics*, 38(4):1–12, 8 2019.

[35] Y. Jung. Multiple predicting K-fold cross-validation for model selection. *Journal of Nonparametric Statistics*, 30(1):197–215, 1 2018.

[36] B. A. Killen, A. Falisse, F. De Groote, and I. Jonkers. In Silico-Enhanced Treatment and Rehabilitation Planning for Patients with Musculoskeletal Disorders: Can Musculoskeletal Modelling and Dynamic Simulations Really Impact Current Clinical Practice? *Applied Sciences*, 10(20):7255, 2020.

[37] M. A. King, C. Wilson, and M. R. Yeadon. Evaluation of a Torque-Driven Model of Jumping for Height. *Journal of Applied Biomechanics*, 22(4):264–274, 2006.

[38] M. A. King and M. R. Yeadon. Determining Subject-Specific Torque Parameters for Use in a Torque-Driven Simulation Model of Dynamic Jumping. *Journal of Applied Biomechanics*, 18(3):207–217, 2002.

[39] M. Kordi, S. Goodall, P. Barratt, N. Rowley, J. Leeder, and G. Howatson. Relation between Peak Power Output in Sprint Cycling and Maximum Voluntary Isometric Torque Production. *Journal of Electromyography and Kinesiology*, 35:95–99, 2017.

[40] K. Kulig, J. G. Andrews, and J. G. Hay. Human Strength Curves. *Exercise and Sport Sciences Reviews*, 12(1), 1984.

[41] F. Lacquaniti and J.F. Soechting. Coordination of arm and wrist motion during a reaching task. *The Journal of Neuroscience*, 2(4):399–408, 4 1982.

[42] D. Landin, J. Myers, M. Thompson, R. Castle, and J. Porter. The role of the biceps brachii in shoulder elevation. *Journal of Electromyography and Kinesiology*, 18(2):270–275, 4 2008.

[43] M. G. C. Lewis, M. R. Yeadon, and M. A. King. Are Torque-Driven Simulation Models of Human Movement Limited by an Assumption of Monoarticularity? *Applied Sciences*, 11(9):3852, 4 2021.

[44] D. G. Lloyd and T. F. Besier. An EMG-driven musculoskeletal model to estimate muscle forces and knee joint moments in vivo. *Journal of Biomechanics*, 36(6):765–776, 2003.

[45] L. Ma, D. Chablat, F. Bennis, and W. Zhang. A new simple dynamic muscle fatigue model and its validation. *International Journal of Industrial Ergonomics*, 39(1):211–220, 1 2009.

[46] S. J. MacKenzie and E. J. Sprigings. A three-dimensional forward dynamics model of the golf swing. *Sports Engineering*, 11(4):165–175, 2009.

[47] A. C. McDonald, S. M. Savoie, D. M. Mulla, and P. J. Keir. Dynamic and static shoulder strength relationship and predictive model. *Applied Ergonomics*, 67:162–169, 2018.

[48] S. A. McErlain-Naylor, M. A. King, and P. J. Felton. A Review of Forward-Dynamics Simulation Models for Predicting Optimal Technique in Maximal Effort Sporting Movements. *Applied Sciences*, 11(4), 2021.

[49] W. McNally. *Forward Dynamic Simulation of a Golf Drive: Optimization of Golfer Biomechanics and Equipment*. PhD thesis, University of Waterloo, 2018.

[50] W. McNally and J. McPhee. Dynamic Optimization of the Golf Swing Using a Six Degree-of-Freedom Biomechanical Model. *Proceedings*, 2(6), 2018.

[51] M. Millard, A. L. Emonds, M. Harant, and K. Mombaur. A reduced muscle model and planar musculoskeletal model fit for the simulation of whole-body movements. *Journal of Biomechanics*, 89:11–20, 2019.

[52] M. Millard, M. Sreenivasa, and K. Mombaur. Predicting the motions and forces of wearable robotic systems using optimal control. *Frontiers in Robotics and AI*, 4:41, 2017.

[53] M. A. Miniato, P. Anand, and M. Varacallo. *Anatomy, shoulder and upper limb, shoulder*. StatPearls Publishing, 2021.

[54] S. Namdari, G. Yagnik, D. D. Ebaugh, S. Nagda, M. L. Ramsey, G. R. Williams, and S. Mehta. Defining functional shoulder range of motion for activities of daily living. *Journal of Shoulder and Elbow Surgery*, 21(9):1177–1183, 2012.

[55] I. J. Pinter, M. F. Bobbert, A. J. van Soest, and J. B. J. Smeets. Isometric torque–angle relationships of the elbow flexors and extensors in the transverse plane. *Journal of Electromyography and Kinesiology*, 20(5):923–931, 2010.

[56] B. C. Prando, C. Carvalho, M. Petrella, and P. R. M. S. Serrão. Test-retest reliability of isometric and isokinetic wrist strength. *Journal of Orthopaedic Science*, 28(1):138–142, 1 2023.

[57] R. Riener and T. Edrich. Identification of passive elastic joint moments in the lower extremities. *Journal of Biomechanics*, 32(5):539–544, 5 1999.

[58] P. Schantz, E. Randall-Fox, W. Hutchison, A. Tyden, and P. Åstrand. Muscle fibre type distribution, muscle cross-sectional area and maximal voluntary strength in humans. *Acta Physiologica Scandinavica*, 117(2):219–226, 1983.

[59] A. Scholz, I. Stavness, M. Sherman, S. Delp, and A. Kecskeméthy. Improved muscle wrapping algorithms using explicit path-error Jacobians. In *Computational Kinematics*, pages 395–403. Springer, 2014.

[60] M. A. Sherman, A. Seth, and S. L. Delp. What is a moment arm? Calculating muscle effectiveness in biomechanical models using generalized coordinates. In *International Design Engineering Technical Conferences and Computers and Information in Engineering Conference*, volume 55973, page V07BT10A052, 2013.

[61] E. J. Sprigings and R. J. Neal. Shifting a portion of the clubshaft's mass distally: does it improve performance? *Sports Engineering*, 4(1):15–21, 2001.

[62] K. M. Steele, A. Seth, J. L. Hicks, M. S. Schwartz, and S. L. Delp. Muscle contributions to support and progression during single-limb stance in crouch gait. *Journal of Biomechanics*, 43(11):2099–2105, 2010.

[63] Y. Suzuki, T. Nomura, M. Casadio, and P. Morasso. Intermittent control with ankle, hip, and mixed strategies during quiet standing: A theoretical proposal based on a double inverted pendulum model. *Journal of Theoretical Biology*, 310:55–79, 10 2012.

[64] A. J. van den Bogert, S. Samorezov, B. L. Davis, and W. A. Smith. Modeling and Optimal Control of an Energy-Storing Prosthetic Knee. *Journal of Biomechanical Engineering*, 134(5), 6 2012.

[65] A. J. van Soest and M. F. Bobbert. The contribution of muscle properties in the control of explosive movements. *Biological Cybernetics*, 69(3):195–204, 1993.

[66] H. E. J. Veeger and F. C. T. van der Helm. Shoulder function: The perfect compromise between mobility and stability. *Journal of Biomechanics*, 40(10):2119–2129, 2007.

[67] S. H. Westing, A. G. Cresswell, and A. Thorstensson. Muscle activation during maximal voluntary eccentric and concentric knee extension. *European Journal of Applied Physiology and Occupational Physiology*, 62(2):104–108, 1991.

[68] S. H. Westing, J. Y. Seger, E. Karlson, and B. Ekblom. Eccentric and concentric torque-velocity characteristics of the quadriceps femoris in man. *European Journal of Applied Physiology and Occupational Physiology*, 58(1-2):100–104, 1988.

[69] S. H. Westing, J. Y. Seger, and A. Thorstensson. Effects of electrical stimulation on eccentric and concentric torque-velocity relationships during knee extension in man. *Acta Physiologica Scandinavica*, 140(1):17–22, 9 1990.

[70] J. Winters. Hill-Based Muscle Models: A Systems Engineering Perspective. In *Multiple muscle systems*, pages 69–93. Springer, 1990.

[71] G. Wu, F. C.T. Van Der Helm, H. E.J. Veeger, M. Makhsous, P. Van Roy, C. Anglin, J. Nagels, A. R. Karduna, K. McQuade, X. Wang, F. W. Werner, and B. Buchholz. ISB recommendation on definitions of joint coordinate systems of various joints for the reporting of human joint motion—Part II: shoulder, elbow, wrist and hand. *Journal of Biomechanics*, 38(5):981–992, 5 2005.

[72] G. T. Yamaguchi. *Dynamic modeling of musculoskeletal motion: a vectorized approach for biomechanical analysis in three dimensions*. Springer, Berlin, 2006.

[73] M. R. Yeadon, M. A. King, and C. Wilson. Modelling the maximum voluntary joint torque/angular velocity relationship in human movement. *Journal of Biomechanics*, 39(3):476–482, 2006.

[74] Y. S. Yoon and J. M. Mansour. The passive elastic moment at the hip. *Journal of Biomechanics*, 15(12):905–910, 1 1982.

[75] Q. Zhang, X. Wang, M. Tian, X. Shen, and Q. Wu. Modeling of Novel Compound Tendon-Sheath Artificial Muscle Inspired by Hill Muscle Model. *IEEE Transactions on Industrial Electronics*, 65(8):6372–6381, 2018.

APPENDICES

Appendix A

Additional Muscle Torque Generator Functions from the Literature

The equations presented below are the torque-angle scaling functions evaluated in [24].

Normal:

$$\tau_\theta(\theta) = \tau_{max} \cdot e^{-\frac{1}{2}\left(6 \cdot \frac{\theta - \theta_0}{ROM}\right)} \tag{A.1}$$

Cosinus:

$$\tau_\theta(\theta) = \tau_{max} \cdot cos\left(\pi \frac{\theta - \theta_0}{ROM}\right) \tag{A.2}$$

Quadratic:

$$\tau_\theta(\theta) = \tau_{max}\left(-4\left(\frac{\theta - \theta_0}{ROM}\right)^2 + 1\right) \tag{A.3}$$

Cubic:

$$\tau_\theta(\theta) = \tau_{max}\left(\frac{27}{4}\left(\frac{\theta - \theta_0}{ROM}\right)^3 - \frac{27}{8}\left(\frac{\theta - \theta_0}{ROM}\right)^2 - \frac{27}{16}\left(\frac{\theta - \theta_0}{ROM}\right) + \frac{27}{32}\right) \tag{A.4}$$

Sinus-Exponential:

$$\tau_\theta(\theta) = \tau_{max}\left(\frac{1}{2}sin\left(1.919\pi e^{\left(-\frac{\theta-\theta_0}{ROM}\right)}+1\right)+\frac{1}{2}\right) \tag{A.5}$$

Appendix B

Muscle Torque Generator Model Parameters

B.1 Completely General Model Parameters

Below are the MTG function parameter results for the completely general 2 DOF MTG model that resulted in the lowest validation error. The lowest error was achieved using Method 3 with the second activation method.

Torque-Angle Scaling Functions

$$\tau_{\theta_1}(\theta_1, \theta_2) = p_{00} + p_{10}\theta_1 + p_{01}\theta_2 + p_{20}\theta_1^2 + p_{11}\theta_1\theta_2 + p_{02}\theta_2^2 + p_{21}\theta_1^2\theta_2 + p_{12}\theta_1\theta_2^2 + p_{03}\theta_2^3$$

Where:

$p_{00} = 1.382$
$p_{10} = -0.01285$
$p_{01} = 0.003759$
$p_{20} = 5.824 \cdot 10^{-5}$
$p_{11} = 4.826 \cdot 10^{-5}$
$p_{02} = -0.0001532$
$p_{21} = -6.313 \cdot 10^{-7}$
$p_{12} = 5.027 \cdot 10^{-7}$
$p_{03} = 7.479 \cdot 10^{-7}$

$$\tau_{\theta_2}(\theta_1, \theta_2) = p_{00} + p_{10}\theta_1 + p_{01}\theta_2 + p_{20}\theta_1^2 + p_{11}\theta_1\theta_2 + p_{02}\theta_2^2 + p_{21}\theta_1^2\theta_2 + p_{12}\theta_1\theta_2^2 + p_{03}\theta_2^3$$

Where:

$p_{00} = 0.513$
$p_{10} = 0.006663$
$p_{01} = 0.00436$
$p_{20} = -4.62 \cdot 10^{-5}$
$p_{11} = -6.117 \cdot 10^{-5}$
$p_{02} = 2.224 \cdot 10^{-5}$
$p_{21} = 8.979 \cdot 10^{-8}$
$p_{12} = 4.298 \cdot 10^{-7}$
$p_{03} = -4.327 \cdot 10^{-7}$

Torque-Velocity Scaling Functions

$$\tau_{\omega_1}(\dot{\theta_1})_{Con} = p_1\dot{\theta_1}^3 + p_2\dot{\theta_1}^2 + p_3\dot{\theta_1} + p_4$$

Where:

$p_1 = -1.919 \cdot 10^{-5}$
$p_2 = 0.001732$
$p_3 = -0.0530$
$p_4 = 1$

$$\tau_{\omega_1}(\dot{\theta_1})_{Ecc} = p_1\dot{\theta_1}^3 + p_2\dot{\theta_1}^2 + p_3\dot{\theta_1} + p_4$$

Where:

$p_1 = 4.485$
$p_2 = 0.003559$
$p_3 = 0.08128$
$p_4 = 1$

$\tau_{\omega_2}(\dot{\theta_2})_{Con} = p_1\dot{\theta_2}^2 + p_2\dot{\theta_2} + p_3$

Where:

$p_1 = 0.0001405$
$p_2 = -0.0111$
$p_3 = 1$

$\tau_{\omega_2}(\dot{\theta_2})_{Ecc} = p_1\dot{\theta_2} + p_2$

Where:

$p_1 = 0.002983$
$p_2 = 1$

Passive Functions

$\tau_{p_1}(\theta_1, \theta_2) = p_{00} + p_{10}\theta_1 + p_{01}\theta_2 + p_{20}\theta_1^2 + p_{11}\theta_1\theta_2 + p_{02}\theta_2^2 + p_{21}\theta_1^2\theta_2 + p_{12}\theta_1\theta_2^2 + p_{03}\theta_2^3$

Where:

$p_{00} = -5.762$
$p_{10} = 0.1067$
$p_{01} = 0.05409$
$p_{20} = -0.0003442$
$p_{11} = -0.003758$
$p_{02} = 0.002334$
$p_{21} = 1.442 \cdot 10^{-5}$
$p_{12} = 5.679 \cdot 10^{-6}$
$p_{03} = -1.791 \cdot 10^{-5}$

$$\tau_{p_2}(\theta_1, \theta_2) = p_{00} + p_{10}\theta_1 + p_{01}\theta_2 + p_{20}\theta_1^2 + p_{11}\theta_1\theta_2 + p_{02}\theta_2^2 + p_{30}\theta_1^3 + p_{21}\theta_1^2\theta_2 + p_{12}\theta_1\theta_2^2$$

Where:

$p_{00} = -1.743$
$p_{10} = -0.06815$
$p_{01} = 0.05989$
$p_{20} = 0.001759$
$p_{11} = -0.001675$
$p_{02} = 0.0002756$
$p_{30} = -8.496 \cdot 10^{-6}$
$p_{21} = 1.041 \cdot 10^{-5}$
$p_{12} = -5.329 \cdot 10^{-6}$

B.2 General Female Model Parameters

Below are the MTG function parameter results for the general female 2 DOF MTG model that resulted in the lowest validation error. The lowest error was achieved using Method 1 with the second activation method.

Torque-Angle Scaling Functions

$$\tau_{\theta_1}(\theta_1)_{70} = p_1\theta_1^3 + p_2\theta_1^2 + p_3\theta_1 + p_4$$

Where:

$p_1 = 9.55 \cdot 10^{-7}$
$p_2 = -0.0001481$
$p_3 = 0.004616$
$p_4 = 0.8126$

$\tau_{\theta_1}(\theta_1)_{85} = p_1\theta_1^3 + p_2\theta_1^2 + p_3\theta_1 + p_4$

Where:

$p_1 = 1.329 \cdot 10^{-6}$
$p_2 = -0.0002045$
$p_3 = 0.006954$
$p_4 = 0.6883$

$\tau_{\theta_1}(\theta_1)_{110} = p_1\theta_1^3 + p_2\theta_1^2 + p_3\theta_1 + p_4$

Where:

$p_1 = 1.598 \cdot 10^{-6}$
$p_2 = -0.0002605$
$p_3 = 0.009392$
$p_4 = 0.6306$

$\tau_{\theta_1}(\theta_1)_{135} = p_1\theta_1^3 + p_2\theta_1^2 + p_3\theta_1 + p_4$

Where:

$p_1 = 7.705 \cdot 10^{-7}$
$p_2 = -9.129 \cdot 10^{-5}$
$p_3 = -0.002348$
$p_4 = 0.8415$

$\tau_{\theta_1}(\theta_1)_{160} = p_1\theta_1^3 + p_2\theta_1^2 + p_3\theta_1 + p_4$

Where:

$p_1 = 9.54 \cdot 10^{-7}$
$p_2 = -0.0001303$
$p_3 = -0.0006366$
$p_4 = 0.8323$

$\tau_{\theta_2}(\theta_2)_0 = p_1\theta_2^2 + p_2\theta_2 + p_3$

Where:

$p_1 = -3.413 \cdot 10^{-5}$
$p_2 = 0.003733$
$p_3 = 0.6712$

$\tau_{\theta_2}(\theta_2)_{30} = p_1\theta_2^2 + p_2\theta_2 + p_3$

Where:

$p_1 = -7.189 \cdot 10^{-5}$
$p_2 = 0.01182$
$p_3 = 0.3333$

$\tau_{\theta_2}(\theta_2)_{60} = p_1\theta_2^2 + p_2\theta_2 + p_3$

Where:

$p_1 = -6.946 \cdot 10^{-5}$
$p_2 = 0.01196$
$p_3 = 0.3334$

$\tau_{\theta_2}(\theta_2)_{90} = p_1\theta_2^2 + p_2\theta_2 + p_3$

Where:

$p_1 = -4.587 \cdot 10^{-5}$
$p_2 = 0.007394$
$p_3 = 0.6123$

$\tau_{\theta_2}(\theta_2)_{120} = p_1\theta_2 + p_2$

Where:

$p_1 = -0.00207$
$p_2 = 1.016$

Torque-Velocity Scaling Functions

$\tau_{\omega_1}(\dot{\theta_1})_{Con} = p_1\dot{\theta_1}^3 + p_2\dot{\theta_1}^2 + p_3\dot{\theta_1} + p_4$

Where:

$p_1 = -3.002 \cdot 10^{-5}$
$p_2 = 0.002519$
$p_3 = -0.06946$
$p_4 = 1$

$\tau_{\omega_1}(\dot{\theta_1})_{Ecc} = p_1\dot{\theta_1}^3 + p_2\dot{\theta_1}^2 + p_3\dot{\theta_1} + p_4$

Where:

$p_1 = 5.868 \cdot 10^{-5}$
$p_2 = 0.004489$
$p_3 = 0.09473$
$p_4 = 1$

$\tau_{\omega_2}(\dot{\theta_2})_{Con} = p_1\dot{\theta_2} + p_2$

Where:

$p_1 = -0.003985$
$p_2 = 1$

$\tau_{\omega_2}(\dot{\theta_2})_{Ecc} = p_1\dot{\theta_2}^2 + p_2\dot{\theta_2} + p_3$

Where:

$p_1 = 0.000158$
$p_2 = 0.01237$
$p_2 = 1$

Passive Functions

$\tau_{p_1}(\theta_1)_{70} = p_1\theta_1 + p_{02}$

Where:

$p_1 = -0.0553$
$p_2 = 0.5671$

$\tau_{p_1}(\theta_1)_{85} = p_1\theta_1^3 + p_2\theta_1^2 + p_3\theta_1 + p_4$

Where:

$p_1 = 0.0003244$
$p_2 = -0.09628$
$p_3 = 9.389$
$p_4 = -305.4$

$\tau_{p_1}(\theta_1)_{110} = p_1\theta_1^3 + p_2\theta_1^2 + p_3\theta_1 + p_4$

Where:

$p_1 = -8.348 \cdot 10^{-6}$
$p_2 = 0.001039$
$p_3 = -0.07717$
$p_4 = 0.7029$

$\tau_{p_1}(\theta_1)_{135} = p_1\theta_1^3 + p_2\theta_1^2 + p_3\theta_1 + p_4$

Where:

$p_1 = -1.521 \cdot 10^{-5}$
$p_2 = 0.002154$
$p_3 = -0.1817$
$p_4 = 7.234$

$\tau_{p_1}(\theta_1)_{160} = p_1\theta_1 + p_2$

Where:

$p_1 = -0.1707$
$p_2 = 13.73$

$\tau_{p_2}(\theta_2)_0 = p_1\theta_2^3 + p_2\theta_2^2 + p_3\theta_2 + p_4$

Where:

$p_1 = -7.265 \cdot 10^{-6}$
$p_2 = 0.001838$
$p_3 = -0.1171$
$p_4 = 0.5502$

$\tau_{p_2}(\theta_2)_{30} = p_1\theta_2^3 + p_2\theta_2^2 + p_3\theta_2 + p_4$

Where:

$p_1 = -7.808 \cdot 10^{-6}$
$p_2 = 0.002128$
$p_3 = -0.1706$
$p_4 = 2.647$

$\tau_{p_2}(\theta_2)_{60} = p_1\theta_2^3 + p_2\theta_2^2 + p_3\theta_2 + p_4$

Where:

$p_1 = -3.937 \cdot 10^{-6}$
$p_2 = 0.001429$
$p_3 = -0.1474$
$p_4 = 2.728$

$\tau_{p_2}(\theta_2)_{90} = p_1\theta_2 + p_2$

Where:

$p_1 = -0.009803$
$p_2 = -1.037$

$\tau_{p_2}(\theta_2)_{120} = p_1\theta_2^3 + p_2\theta_2^2 + p_3\theta_2 + p_4$

Where:

$p_1 = -8.568 \cdot 10^{-6}$
$p_2 = 0.003841$
$p_3 = -0.5079$
$p_4 = 16.21$

B.3 General Male Model Parameters

Below are the MTG function parameter results for the general male 2 DOF MTG model that resulted in the lowest validation error. The lowest error was achieved using Method 2 using the first activation method.

Torque-Angle Scaling Functions

$\tau_{\theta_1}(\theta_1, \theta_2) = p_{00} + p_{10}\theta_1 + p_{01}\theta_2 + p_{20}\theta_1^2 + p_{11}\theta_1\theta_2 + p_{02}\theta_2^2 + p_{21}\theta_1^2\theta_2 + p_{12}\theta_1\theta_2^2 + p_{03}\theta_2^3$

Where:

$p_{00} = 1.447$
$p_{10} = -0.01379$
$p_{01} = -0.0005368$
$p_{20} = 5.97 \cdot 10^{-5}$
$p_{11} = 9.887 \cdot 10^{-5}$
$p_{02} = -0.0001232$
$p_{21} = -8.866 \cdot 10^{-7}$
$p_{12} = 6.613 \cdot 10^{-7}$
$p_{03} = 4.955 \cdot 10^{-7}$

$$\tau_{\theta_2}(\theta_1, \theta_2) = p_{00} + p_{10}\theta_1 + p_{01}\theta_2 + p_{20}\theta_1^2 + p_{11}\theta_1\theta_2 + p_{02}\theta_2^2 + p_{21}\theta_1^2\theta_2 + p_{12}\theta_1\theta_2^2 + p_{03}\theta_2^3$$

Where:

$p_{00} = 0.6179$
$p_{10} = 0.00407$
$p_{01} = 0.00683$
$p_{20} = -3.269 \cdot 10^{-5}$
$p_{11} = -7.839 \cdot 10^{-5}$
$p_{02} = 1.882 \cdot 10^{-6}$
$p_{21} = -2.069 \cdot 10^{-8}$
$p_{12} = 7.295 \cdot 10^{-7}$
$p_{03} = -5.043 \cdot 10^{-7}$

Torque-Velocity Scaling Functions

$$\tau_{\omega_1}(\dot{\theta_1})_{Con} = p_1\dot{\theta_1}^3 + p_2\dot{\theta_1}^2 + p_3\dot{\theta_1} + p_4$$

Where:

$p_1 = -1.142 \cdot 10^{-5}$
$p_2 = 0.001199$
$p_3 = -0.04318$
$p_4 = 1$

$$\tau_{\omega_1}(\dot{\theta_1})_{Ecc} = p_1\dot{\theta_1}^3 + p_2\dot{\theta_1}^2 + p_3\dot{\theta_1} + p_4$$

Where:

$p_1 = 3.768 \cdot 10^{-5}$
$p_2 = 0.003126$
$p_3 = 0.07683$
$p_4 = 1$

$\tau_{\omega_2}(\dot{\theta_2})_{Con} = p_1\dot{\theta_2}^2 + p_2\dot{\theta_2} + p_3$

Where:

$p_1 = 0.0002403$
$p_2 = 0.01668$
$p_3 = 1$

$\tau_{\omega_2}(\dot{\theta_2})_{Ecc} = p_1\dot{\theta_2} + p_2$

Where:

$p_1 = -0.0001378$
$p_2 = 1$

Passive Functions

$\tau_{p_1}(\theta_1, \theta_2) = p_{00} + p_{10}\theta_1 + p_{01}\theta_2$

Where:

$p_{00} = -2.379$
$p_{10} = 0.03088$
$p_{01} = -0.0509$

$$\tau_{p_2}(\theta_1, \theta_2) = p_{00} + p_{10}\theta_1 + p_{01}\theta_2 + p_{20}\theta_1^2 + p_{11}\theta_1\theta_2 + p_{02}\theta_2^2 + p_{30}\theta_1^3 + p_{21}\theta_1^2\theta_2 + p_{12}\theta_1\theta_2^2$$

Where:

$p_{00} = -3.183$
$p_{10} = -0.04959$
$p_{01} = 0.02993$
$p_{20} = 0.002002$
$p_{11} = -0.001316$
$p_{02} = 0.0006157$
$p_{30} = -1.068 \cdot 10^{-5}$
$p_{21} = 1.114 \cdot 10^{-5}$
$p_{12} = -9.877 \cdot 10^{-6}$